Indo-Atlantic Exchange, Mesoscale Dynamics, and Antarctic Intermediate Water

Tonia Astrid Capuano, Sabrina Speich, Xavier Carton, Remi Laxenaire

AGU100 ADVANCING EARTH AND SPACE SCIENCE

JGR

Journal of Geophysical Research: Oceans

RESEARCH ARTICLE
10.1002/2017JC013521

Indo-Atlantic Exchange, Mesoscale Dynamics, and Antarctic Intermediate Water

Tonia Astrid Capuano[1], Sabrina Speich[2], Xavier Carton[1], and Remi Laxenaire[3]

[1]Laboratoire d'Ocanographie Physique et Spatiale, LOPS-UBO, Brest, France, [2]Laboratoire de Meteorologie Dynamique, LMD-IPSL, Ecole Normale Superieure, Paris, France, [3]Laboratoire de Meteorologie Dynamique, UMR 8539 Ecole Polytechnique, ENS, CNRS, Paris, France

Key Points:
- High horizontal and vertical numerical resolutions required to depict the Cape Basin turbulent dynamics
- Key role of the Agulhas eddies in the advection of AAIW properties and associated thermohaline transport
- The regional mesoscale processes are characterized by a strong seasonality

Supporting Information:
- Supporting Information S1

Correspondence to:
S. Speich,
speich@lmd.ens.fr

Citation:
Capuano, T. A., Speich, S., Carton, X., & Laxenaire, R. (2018). Indo-Atlantic exchange, mesoscale dynamics, and Antarctic intermediate water. *Journal of Geophysical Research: Oceans*, *123*, 3286–3306. https://doi.org/10.1002/2017JC013521

Received 2 OCT 2017
Accepted 8 MAR 2018
Accepted article online 6 APR 2018
Published online 9 MAY 2018

Abstract This study evaluates the capability of eddy-permitting regional ocean models to reproduce the interocean exchange south of Africa. In this highly turbulent region, we show that the vertical structure of the horizontal flows need to be appropriately resolved to realistically advect thermocline water masses into the South Atlantic. Our results point out that a grid-spacing of 1/24° on the horizontal and 50 m on the vertical homogeneously distributed are required to account for a correct transport of surface and subsurface water masses properties and their in-route transformation by mixing. Preliminary Lagrangian analyses highlight the primary role of the upper-ocean mesoscale eddies on water masses transport and fate, with a particular emphasis on Antarctic Intermediate Waters (AAIWs) dynamics and characteristics. We evaluate the numerical results against observations (AVISO data and Argo floats profiles). Modeled and observed eddies were examined in number, polarity, size, trajectory, and for their contribution to AAIW properties. A clear asymmetry, in number and radius, emerges between cyclones and anticyclones. The high-resolution simulation was the most energetic, with more abundant and smaller structures than those detected in AVISO. However, eddy statistics compare reasonably well in terms of mean pathways when restricted to Agulhas Rings, which are on average quasi-Gaussian in shape. Regionally, the Ertel potential vorticity anomaly is marked at the surface by a temporal variability with winter intensification, directly reflected in the seasonal cycle of the eddies number. Noting the growth of the baroclinic Rossby radius in winter, this suggests baroclinic processes as essential for these eddies generation.

1. Introduction

South of Africa is the open gateway for the global Meridional Overturning Circulation (MOC) that provides the export channel for the North Atlantic Deep Water (NADW) to the global ocean and the counterbalancing water transport to the North Atlantic importing heat and salt from the Indian and Pacific Oceans (Gordon et al., 1992; Speich et al., 2007). This region is influenced by the largest levels of turbulence observed in the world ocean, being the confluence area of intense large-scale currents: the eastward flowing Antarctic Circumpolar Current (ACC), the South-Atlantic Current (SAC), and the Agulhas Current (AC), all later converging through the Cape Basin into the Benguela Current (Gordon et al., 1992, 2001).

The AC flows south and then westward around the southern-east rim of Africa, with an annual mean volume flux to the sea bottom at 30°E of 75 Sv (Bryden & Beal, 2001). South of Africa (15°E–20°E) the Agulhas waters curl back to the Indian Ocean, forming the Agulhas Retroflection, whose significant role does not end with its momentary loop into the southeast corner of the South Atlantic: there is considerable transfer of Indian Ocean water into the upper kilometer of the Atlantic, often referred to as the Agulhas leakage (Lutjeharms, 2006).

Pioneering modeling studies have revealed the potential impact of this leakage on the strength and stability of the Atlantic MOC (AMOC) (Biastoch et al., 2008; Weijer et al., 1999) and the global-scale oceanic circulation associated to it. This impact is strongly dependent on how the characteristics (temperature, salinity, and potential vorticity) of the various waters, leaking from the Indian Ocean to the Atlantic, mix and blend in the Cape Basin through jets, meanders, eddies and filaments, determining the contribution of the leakage in the broader scale MOC. There is mounting, scientific evidence that these local, mesoscale, and submesoscale interactions could actually constitute the major link between the South-Atlantic Ocean and the global MOC (Biastoch et al., 2008). In particular, a highly energetic field of coexisting anticyclonic and cyclonic

eddies has been documented: Agulhas Rings of typically 70–200 km diameter have been observed to merge, split, deform, and to reconnect to the Agulhas Retroflection (Boebel et al., 2003). Concomitant, slightly smaller cyclones seem to drift across the northwestward migration path of the Agulhas Rings (Boebel et al., 2003; Chelton et al., 2011; Morrow et al., 2004). These cyclones, with typical diameters of 60–120 km, are formed within the Cape Basin along the African shelf, inshore of the AC, and in the subantarctic region south of Africa (Boebel et al., 2003). Oceanographers have for long time looked at this region as an area where "*. . .isolated Agulhas Rings embedded in a sluggish Benguela Drift. . .*." This concept has been recently revisited by Boebel et al. (2003), who proposed to rename the Cape Basin as Cape Cauldron to indicate the highly energetic field of coexisting anticyclonic and cyclonic eddies, which continuously interact with each other, in a general environment of vigorous stirring and mixing. In addition, Matano and Beier (2003) have suggested a subsurface intensification of both cyclones and anticyclones in this region, meaning that their dynamical signature would be able to fluence also the thermohaline properties of water masses at depth (Schmid et al., 2003).

The Cape Basin is actually so efficient in terms of mixing that Antarctic Intermediate Water (AAIW), inflowing from the Indian and South-Atlantic oceans, gets locally modified in three regional varieties: Atlantic AAIW (A-AAIW, characterized by $S \leq 34.2$), Indian AAIW (I-AAIW, $S \geq 34.3$), and Indo-Atlantic intermediate water (IA-AAIW, $34.2 < S < 34.3$) (Rusciano et al., 2012). Modeling results associated to Lagrangian diagnostics confirmed that local dynamics generate an important mixing of remote AAIW varieties within the Cape Basin (Rimaud et al., 2012). However, this numerical study, as well as any other focusing on this region, was performed at a maximum horizontal grid-spacing of 1/12°, that is at about 7.3 km, an insufficient resolution to correctly reproduce the mesoscale dynamics (Levy et al., 2010). Indeed, the recent work of Soufflet et al. (2016) showed that, in the case of the Regional Ocean Model System (ROMS) used here, the effective resolution is approximately equal to $7\Delta x$ (being Δx the horizontal grid point spacing of the model), since dynamics of smaller lengthscales appear to be unsupported by the model simulations. This means that for numerical simulations at 1/12°, the effective horizontal resolution is closed to 50 km rather than 8. Given that the local internal radius of deformation is about 30 km (Chelton et al., 1998), a model resolution 2 or 3 times higher than 1/12° is required to improve the reliability of the simulated mesoscale field, even if the simulation of a realistic energy cascade and processes spectrum would require a much higher resolution to resolve the submesoscale dynamics (Capet et al., 2008).

In this article, we focus on how the Indo-Atlantic interocean exchange and the Cape Basin dynamics improve in a regional simulation by including smaller spatial scales, in order to better resolve the strongly nonlinear processes and qualify their impact on the thermohaline structure of AAIW. Given that the Cape Basin mesoscale eddies represent the principal means of transport of thermocline and intermediate waters between the Indian and Atlantic ocean, our main scientific objectives will be: (1) to quantitatively assess how much the representation of the local thermohaline distribution and energetics improves, at the surface and in the subsurface, when increasing the model resolution, both vertically and horizontally; (2) to statistically characterize the modeled mesoscale field in comparison to altimetric gridded product; (3) to investigate if a specific temporal variability distinguishes the regional mesoscale field; and (4) evaluate their contribution to the advection of the AAIW T-S properties in our study region. Each of these questions will be discussed in a dedicated subsection of this article.

In the following, we will first introduce, in section 2, the methods we have implemented for addressing our study objectives, as well as the data set of in situ and satellite observations used in conjunction with our model output. In section 3, we will first present an extensive comparison of the numerical simulations, in terms of their skill in reproducing both the observed thermohaline properties and dynamics. We will then describe the analyses of the mesoscale eddies sensitivity to changes in the model resolution, providing evidence of a temporal-dependent behavior and assessing their impact on the water mass properties, mixing, and transport. In the last section, we will summarize the results and draw the major conclusions of this study.

2. Data and Methods

2.1. The Ocean Model

The methodology chosen in this work was to run realistic numerical simulations of the ocean circulation around Southern Africa, using the UCLA-IRD version of ROMS (http://www.romsagrif.org/), which is a free

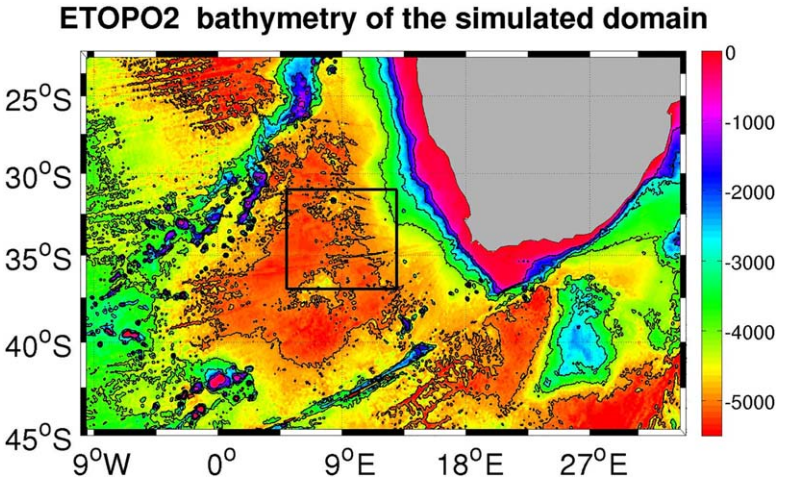

Figure 1. The map shows geographical domain we used to implement the ROMS regional simulations. The color shading displays the bottom topography (m) from the Etopo2 data set (Smith & Sandwell, 1997). The square represents the box in the Cape Basin where several analysis were carried out.

surface, primitive-equation ocean model. We refer to Shchepetkin and McWilliams (2005), for a detailed description of the numerical model, even though it is worth mentioning here a few technical characteristics that have important effects on the model capability of properly reproducing coastal dynamics. ROMS uses a terrain-following vertical coordinate system that allows a more realistic representation of the local bathymetry, compared to z-levels models. This is a key factor when studying an oceanic region like the Cape Basin, where the ocean topography has been shown to be very influential on the interocean exchanges (Speich et al., 2006). The bathymetry (h) used in this model has been filtered in order to keep a slope parameter "r" (= $\Delta h/2h$, ratio of the difference in depth to twice the depth) smaller than a given value (0.25 in our case). This topographic filtering ensures the avoidance of eventual inconsistencies which could occur in the approximation of the horizontal pressure gradient terms, when these are transformed in sigma-coordinates (Shchepetkin & McWilliams, 2003). In addition, the ROMS grid is isotropic and does not introduce any asymmetry in the horizontal dissipation of turbulence, allowing a fair representation of mesoscale dynamics (Speich et al., 2006).

Our simulated domain extends from 10°W to 34°E and from 22°S to 45°S (Figure 1). The five simulations under examination in this paper are listed in Table 1 and were designed using different horizontal and vertical resolutions: from 1/12° to 1/24°, against 32, 64, and 100 vertical levels, in order to increasingly better resolve the baroclinic modes of the study region, not only in the horizontal but also along the water column (Stewart et al., 2017). To better depict the characteristics of the local water masses at depth, we performed changes in the model vertical stretching parameters, that control the distribution of sigma levels, in our last three simulations (namely AGU_12_64_H, AGU_24_64_H, and AGU_24_100_H, dubbed with "H" for homogeneous). This allows the vertical levels to be more uniformly spaced, instead of being concentrated in the

Table 1
Table Summarizing the Technical Features of the Five Simulations Here Presented

Name of the simulation	Horizontal resolution	Sigma levels	Sigma levels distribution	S RMSE	σ difference	Q RMSE
1/12_32	1/12°, ~7.3 km	32	Surface-stretched	0.065	0.046	0.074
1/12_64	1/12°, ~7.3 km	64	Surface-stretched	0.064	0.038	0.062
1/12_64_H	1/24°, ~7.3 km	64	Homogeneously stretched	0.053	0.026	0.055
1/24_64_H	1/24°, ~3.6 km	64	Homogeneously stretched	0.037	0.021	0.048
1/24_100_H	1/24°, ~3.6 km	100	Homogeneously stretched	0.032	0.016	0.041

Note. The fifth and seventh columns show the RMSE values of the difference between each simulation and Argo data in terms of the salinity distribution of Figure 3 and the Q estimate of Figure 4. The values of the sixth column represent the difference in potential density (σ) between its mean value at a given level and the following one for each run.

upper layers (the default model configuration). Moreover, in the highest resolution simulation (AGU24_100_H) we also made use of a recently introduced function optimizing the sigma levels, designed to impose a more homogeneous distribution of these levels, in respect to its original definition (Lemarie et al., 2012). This new function acts to smooth the tracer fields (T and S) and to filter out the slight, spurious numerical noise that we experimented in our first four runs, due to the use of the advection scheme rotated along the isopycnals (RSUP3) (Marchesiello et al., 2009). The choice of these numerical options in the vertical distribution of the sigma levels, enabled us to gain a significant improvement in the representation of the isopycnal interfaces within the water masses, as we will further discuss in section 3.

To easily compare the different configurations of Table 1, we used the following data sets and conditions to create the mesh grid, the forcings at the open boundaries and the initial state:

Bathymetry (h) is derived from the ETOPO2 data set (Smith & Sandwell, 1997) and smoothed under the constraint that "r" < 0.25 with the minimum depth represented at 10 m. At the surface, wind forcing, heat, and freshwaters sources were extracted from the COADS climatology (Da Silva et al., 1994), in accordance with our focus on the investigation of intrinsic, oceanic variability. At the lateral open boundaries, an active, implicit, upstream biased radiation condition connected the model solution to the surrounding ocean (Marchesiello et al., 2001). The ocean was set initially at rest, with temperature and salinity fields taken from the World Ocean Atlas 2009 data set (WOA09) (Locarnini et al., 2010) at 1° of resolution.

All the simulations were run for 5 years and the steady state was statistically achieved after a spin-up period of roughly 1 year, after which the surface-averaged kinetic energy approached a stable level and started to exhibit fluctuations. At the end of this short spin-up, the volume integrated temperature and salinity did not present any significant temporal drift.

In order to evaluate the effect of other background values, like the horizontal diffusion or the bottom drag coefficient, as well as the topographically influent slope parameter "r," several simulations were run at very low resolution (1/4°). This allowed us to test the sensitivity of the model to slight alterations in its initial parameters and to subsequently address the choice of the best configuration to use for running higher resolution simulations. It will be on these latter runs that our presentation of results and discussion will focus hereafter. The rest of this section will describe the observations data sets used to validate our numerical configurations, the eddy detection and tracking algorithm used to assess the simulated mesoscale eddies and the potential vorticity budget applied to investigate the mesoscale dynamics.

2.2. Observational Data Sets for Model Comparison

Twelve years of in situ observations (from the beginning of December 2000 to the end of December 2012) from the Argo program—a global array of free-drifting profiling floats that measure temperature and salinity within the upper 2,000 m of the ocean—were retrieved from the Coriolis Data Center (http://www.coriolis.eu.org: http://doi.org/10.17882/42182). For the comparison with the model reproduction of AAIW, we used the gridded version of this data set as created by Rusciano et al. (2012), where data were grouped and averaged in 1° longitude by 1° latitude boxes within the simulated domain. While, for the comparison of the modeled θ–S and available potential energy distributions at depth, the raw data of the profilers were employed, using exclusively those in the delayed mode as their salinity has been adjusted by comparison with other measurements. Only data with control quality flags 1 and 2, that refer to "good observation" and "probably good observation," were kept.

We also took advantage of the daily gridded, altimetry data, produced by Ssalto/Duacs and distributed by AVISO, with support from CNES, after being interpolated over a homogeneous 1/4° grid. These data were used to validate the energy content of our simulations at the surface and compare the results of the eddy detection of our model output with the same results from the AVISO product. The latter consists of 16 years (from January 2000 to December 2015) of altimetric retrieved observations and represents a multimission product, deriving from the combination of all satellite data available at one time (Jason-1, Envisat, GFO, ERS-1, ERS-2, and Topex/Poseidon). We made use of the latest version of the AVISO Ssalto-Duacs altimetric product (Duacs/AVISO, 2014).

2.3. Algorithm of Eddy Detection and Tracking

For localizing eddies at the surface and exploring the differences in shape, number, and size between the five simulations, along with those in the characteristics of the intermediate waters trapped within these

structures, we applied to our model outputs the detection and tracking methodology of Chaigneau et al. (2008, 2011), further developed by Pegliasco et al. (2015). Their approach is similar to the one of Chelton et al. (2011) for identifying and extracting eddies from the geophysical turbulent flow, since they are both based on geometric criteria, in opposition to other methods based on physical properties. The original method of Chaigneau et al. (2008) hinges on the search of the outermost closed contour of Sea Level Anomaly (SLA) around extremes of AVISO Ssalto-Duacs Mapped SLA (Ducet et al., 2000; Pascual et al., 2006). In the case of our simulations, we used a set of Sea Surface Height (SSH) maps, taken as daily snapshots from the last 3 years of each of our simulations, in order to allow them to reach a full statistical adjustment.

The first step of the analysis consists in the detection of possible centers of cyclones (anticyclones) that are associated with local minima (maxima) of SSH. The detection of the extrema is done separately for the minima and maxima, with a moving window set to $1^\circ \times 1^\circ$ width in this study. In a second step, extrema centered in $6^\circ \times 6^\circ$ squares, where closed contours of SSH have been identified, are individually studied. The outermost contours around minima (maxima), containing only one local extremum, are classified as the outer limit of each eddy. This limit is used to define the eddy amplitude, which corresponds to the modulus of the SSH difference between the center and the outermost contours. Identified extrema associated with amplitude lower than 1 cm are rejected. This allows to prevent the separation of one large eddy into two or more smaller features at one given time step.

Another particularity of this technique worth mentioning is that the detected contours of all the eddies are stored and can be used later to define their trajectories. Some basic properties for each eddy are computed such as their amplitude, area and equivalent radius for a circle. Beside the restriction applied on the eddies amplitude, a temporal filter is used after the completion of the eddies tracking. The latter is based on the superimposition of contours between 2 successive days and enables us to define trajectories of both cyclones and anticyclones. Here a minimum lifetime of 7 days is set for all trajectories, thus all the eddies which last less than 7 days before a merging or after a splitting event are also removed. By these two criteria, we avoid spurious detections and the remaining structures are classified as either cyclonic or anticyclonic. For the latter, we have estimated some of their statistical properties (e.g., number, radius, shape, and trajectory) and looked at the AAIW's characteristics within the eddies crossing the Cape Basin.

2.4. Potential Vorticity

The Ertel Potential Vorticity (Ertel, 1942) has the following mathematical form:

$$EPV = -\frac{1}{\rho}\left((f+\omega)\frac{\partial \rho}{\partial z} - \left(\frac{\partial v}{\partial z}\frac{\partial \rho}{\partial x}\right) + \left(\frac{\partial u}{\partial z}\frac{\partial \rho}{\partial y}\right)\right) \quad (1)$$

where ρ is the potential density, f is the Coriolis parameter ($f = 2\Omega\sin\phi$), ω is the vertical component of the relative vorticity ($\partial v/\partial x - \partial u/\partial y$), $\partial\rho/\partial z$ represents the stratification, which combined all together constitute the vertical components of the Ertel PV, namely the sum of the relative vorticity (ω) and the vortex stretching ($f * \partial\rho/\partial z$) terms. The last two terms of the RHS are the sum of the horizontal components of the Ertel PV in the x and y directions, where the terms of the zonal and meridional shear ($\partial u/\partial z$ and $\partial v/\partial z$) are multiplied by the lateral gradients of density ($\partial\rho/\partial x$ and $\partial\rho/\partial y$).

Potential vorticity (PV) analyses provide essential information on mesoscale flows. Marchesiello et al. (2003) showed that significant departures from the Sverdrup balance occur in the California Current System and are mainly due to the effect of the PV vertical terms. In our area of interest, given the regional high level of turbulence characterizing the Agulhas System, we expect the PV vertical terms to be important. Moreover, PV analyses can help distinguish the origin of water masses within the Agulhas System (e.g., AAIW is characterized by a relative PV maximum, Talley, 1996).

The Ertel PV (EPV hereafter) is adiabatically conserved along isopycnals in a Lagrangian sense, meaning that it can only be changed by diabatic or frictional processes. The EPV is thus a useful tracer for the identification of filaments, meanders, smaller vortices, and fronts and looking separately at each of its components allows to better apprehend their scales and intensity. At large scale, these terms are quite negligible, if taken separately, but at mesoscale or smaller scales, their magnitude becomes relevant, above all in presence of fronts. Since they are also related to the development of instabilities, quantifying their respective intensity and spatiotemporal distribution could help shedding some light on these nonlinear processes.

In the following section, we will describe the horizontal distributions of the vortex stretching (Q hereafter) and the relative vorticity (ω) terms, as means of further validating and discriminating our simulations; time series of the EPV anomaly and its vertical components will be discussed in relation to eddies temporal trends.

3. Results

To evaluate the realism of our ROMS simulations and to qualify the impact of the mesoscale processes on the regional dynamics, we have undertaken various comparisons with different data sets. Even though the focus of our study is on the dynamics of intermediate waters, we have first validated our numerical simulations against surface observations (satellite and in situ data); indeed, subsurface observations are still very sparse.

3.1. Surface Dynamics and Thermohaline Structure

As expected from previous high-resolution numerical studies (Capet et al., 2008; Molemaker et al., 2015; Rosso et al., 2014), we observe a gradual improvement in the way our model reproduces the main features and characteristics of the surface circulation, in terms of the T-S variables and modeled dynamics, as we increase the vertical and horizontal resolutions (supporting information Figures S1 and S2). All the simulations are able to capture the large-scale features of the greater Agulhas System. However, the two higher resolution runs (at 1/24°) exhibit surface temperature and height fields with closer agreement to the observations, capturing in particular the higher values shown in the observations over the Agulhas Plateau. Concerning the alongshore Agulhas Current temperature, salinity, and energy inflow from the Indian Ocean into the Southeast Atlantic, the lowest horizontal resolution simulations (AGU12_32, AGU12_64, and AGU12_64_H) tend to overestimate the averages of the analyzed surface variables, especially in areas close to the South-African west coast and around the Agulhas Retroflection.

Noteworthy are also the differences discernible between the numerical experiments having a homogeneous distribution of the vertical levels (AGU12_64_H, AGU24_64_H, and AGU24_100_H) with those characterized by a higher vertical resolution in the upper layers (AGU12_32 and AGU12_64). The homogeneous distribution of vertical levels increases the vertical resolution at depth. This induces a reduction in the discrepancies between the model surface fields and the observational products, attenuating those warm biases event at the lowest horizontal resolution. While this improvement is not major if only the number of vertical levels is increased (e.g., AGU12_32 versus AGU12_64), as this increase concerns only the upper 200 m of the ocean, it indicates that the vertical resolution of the model is as important as the horizontal one to reproduce more realistic surface dynamics and thermohaline distributions.

3.2. Water Masses Properties at Depth

Figure 2 shows the Potential Temperature-Salinity (θ–S) diagrams for the whole domain and for waters at intermediate and deep levels (i.e., $\theta < 10$°C), where every dot represents the θ–S values extracted at each grid point of the model. The values are scattered in red color for the lowest resolution simulation (AGU12_32, Figure 2a) and in cyan for the highest resolution one (AGU24_100_H, Figure 2b). The overlaid blue curves represent the mean (continuous line) and standard deviation (dotted lines) values from Argo data.

These diagrams show the main water masses circulating, at depth, within the greater Agulhas Current System and Cape Basin. The highest values of θ and S correspond to the warmer and more saline waters inflowing from the Indian Ocean; the center of the diagram is occupied by intermediate waters (AAIW of both Indian and Atlantic origins, see Rusciano et al., 2012), while the lowest part of the plot indicates the presence of deep and bottom waters (NADW, CDW, and modified AABW; these waters appear only in the model data as Argo profiles do not exceed 2,000 dbar), characterized by higher values of S and lower θ than AAIW.

The simulations with the lowest horizontal and vertical resolutions (AGU12_32, in Figures 2a, and AGU12_64) show, for all the water masses, a wider θ–S range than the higher resolution solutions and observations. The simulation with increased vertical resolution in the subsurface and deep layers (AGU12_64_H, not shown here) presents a behavior closer to observations than the two previous experiments. In fact, the differences between AGU12_64 and AGU12_64_H are larger compared to that between AGU12_32 and AGU12_64, which almost completely overlap (not shown). The latter are more diffusive, leading to values of θ and S very different from those measured by Argo or found in the higher vertical resolution simulations. In particular, their salinity minimum, intersecting the 27.05 isopycnal, is of ~33.7 psu.

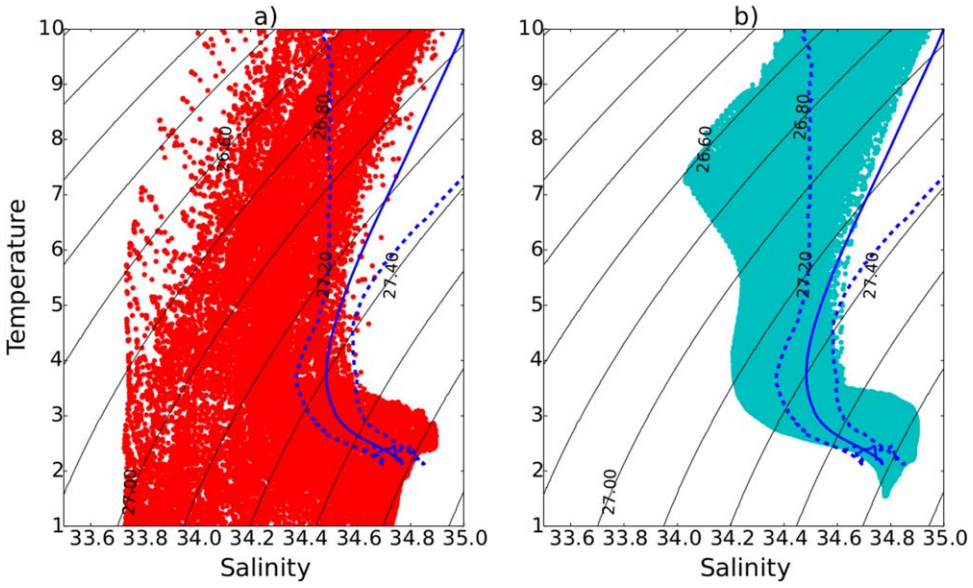

Figure 2. The θ–S distribution for (a) the lowest resolution simulation (AGU12_32) and for (b) the highest resolution simulation (AGU24_100_H) for the whole domain. In both diagrams, are also presented the θ–S mean and standard deviation (in blue, continuous and dotted lines) from Argo data for subsurface and deep waters (defined as those having a value of $\theta < 10$°C).

These values differ from the regional observed AAIW minimum of salinity (around 34.3 psu) and from the typical range of potential density anomaly (27.2–27.6 kg/m^3) of Argo data. The water masses properties in the whole set of simulations with homogeneous vertical levels distribution are better preserved, even though a discrepancy persists between the thermohaline distributions of these numerical experiments and the one from Argo, especially at the level of the central waters (Figure 2b). This shift in θ–S is probably to ascribe to the lack of more realistic, synoptic forcings at the lateral and surface boundaries of our simulations. However, since the focus of our study is on the full range of water masses accomplishing the Indo-Atlantic exchange, and particularly on AAIW, we can affirm that a reasonable agreement between water masses properties in AGU24_100_H and in observations has been achieved for these layers. Such a modeling improvement is confirmed by the estimation of the root-mean-squared error (RMSE) of the difference in mean salinity between each simulation output and Argo, whose value slowly reduces from AGU12_32 to AGU24_100_H (see fifth column of Table 1).

By augmenting the number of sigma levels and by homogenizing their vertical distribution, also the difference in potential density between its mean value at a given level and the following one substantially decreases from the lowest to the highest resolution simulation (see sixth column of Table 1). Thus, a higher vertical resolution at the subsurface and in the deep ocean better reproduces the vertical thermohaline structure of the water column. This is true for the simulation at the lowest horizontal resolution (AGU12_64_H) and it is even more remarkable at higher, horizontal and vertical resolutions (AGU24_64_H and AGU24_100_H). Both aspects are therefore essential for a correct representation of thermocline water masses, and, in particular of AAIW.

3.3. Agulhas Leakage and Related AAIW Characteristics

To acquire a more quantitative insight on the model capability of capturing the AAIW characteristics and dynamics, we carried out various analyses along the 27.2 isopycnal. The latter constitutes the typical potential density surface for this water mass in the Southwest Indian and Southeast Atlantic oceans (Piola & Gordon, 1989; Reid, 1989; Talley, 1996).

Figure 4 displays the linear vortex stretching term (Q) in the EPV (first term on the RHS of equation (1)), computed from Argo data (Figure 3a) and estimated averaging daily means over the last 3 years of each simulation (Figures 3b–3f). The Argo climatology shows the already documented regional pattern for the AAIW Q: a maximum characterizing the Agulhas Current system and a high-Q tongue originating from the Agulhas Retroflection and progressing northwestward across the Cape Basin, after undergoing a sharp transition due to the local intense mixing of I-AAIW with A-AAIW (Rusciano et al., 2012; Talley, 1996). Only the

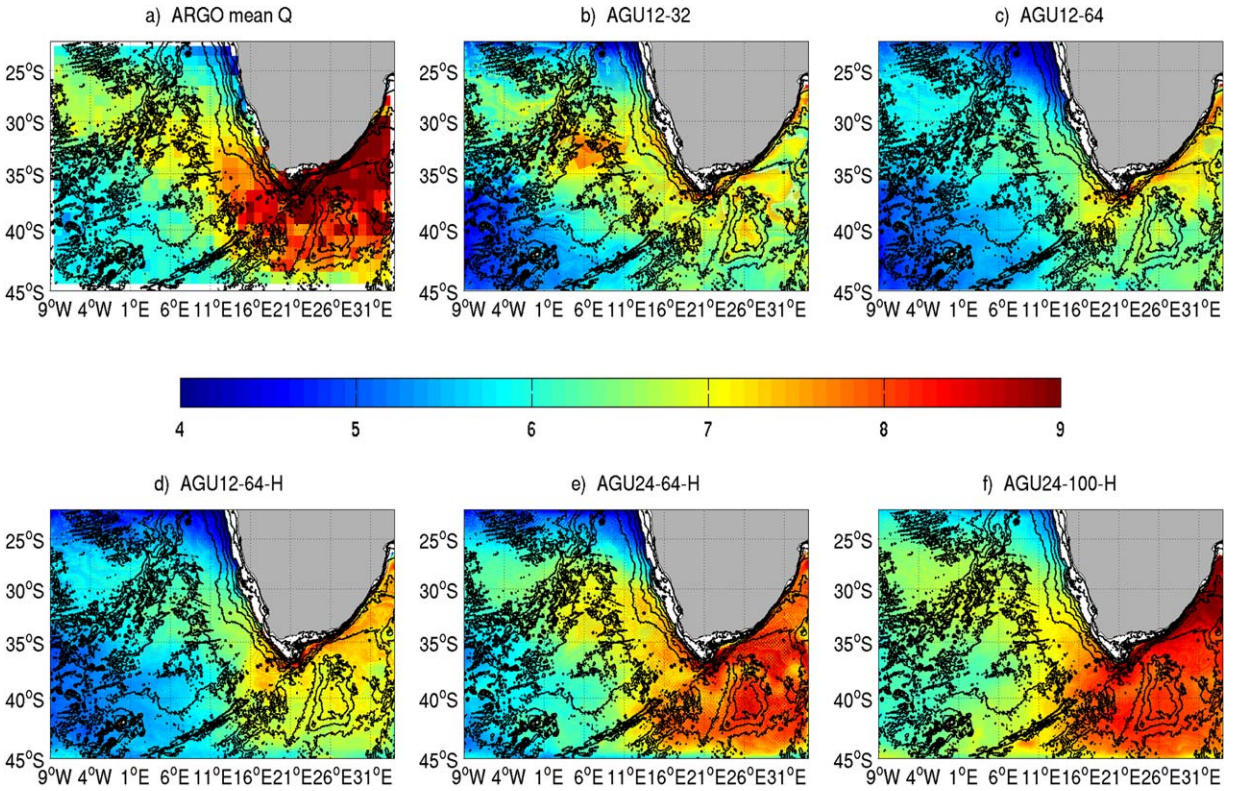

Figure 3. The average of the linear vortex stretching term (Q, [$m^{-1}\ s^{-1} \times 10^{-11}$]) extracted along the 27.2 isopycnal for (a) the Argo climatology and (b–f) the different model configurations. Black contours represent the −5,000, −4,000, −3,000, −2,000, −1,000, −500, −200, −100 m isobaths from the Etopo2 data set (Smith & Sandwell, 1997).

simulations at 1/24° (Figures 3e and 3f) correctly represent such a behavior, while the lower resolution simulations (AGU12_32 and AGU_12_64, Figures 3b and 3c) do not show a contrast in Q between the two oceans nor a maximum for the Agulhas Current system AAIW. The transition in Q starts to appear in AGU12_64_H (Figure 3d) and it gains in realism in AGU24_64_H and AGU24_100_H. This improvement with resolution has been quantified through the RMSE of the difference in Q between the model estimates and Argo for each run (see seventh column of Table 1).

These results emphasize the model capability at the highest resolutions to correctly reproduce the regional stratification of AAIW, as well as their advection and mixing. In this regard, a sufficient vertical resolution at depth is mandatory to resolve the nonlinear dynamics of the Agulhas Retroflection and leakage. The more viscous dynamical behavior of the lowest resolution simulations and their vertical inadequacy to realistically depict the water masses characteristics lead to the incorrect representation, transport and mixing of T-S properties between the Indian and the Atlantic water masses. In fact, an appropriate increase of the vertical resolution complements the resolution capabilities of the horizontal grid (Stewart et al., 2017). Barnier et al. (1991) have indeed demonstrated that models at coarse vertical resolutions fail to reproduce baroclinic modes higher than the first two; albeit these high modes have low kinetic energy content, they play a catalytic role in the eddy-driven circulation. In the next, we will thus analyze the effects of our model resolutions on the simulated mesoscale dynamics.

3.4. Energy Content of the Mesoscale Eddy Field

Here we focus on eddy energy budgets to quantitatively assess the way in which our simulations picture the regional mesoscale processes, as they play a leading role in regulating the Indo-Atlantic exchange. The eddy kinetic energy (EKE) filed has been widely observed with the global coverage of satellite altimetry measurements and we use the root-mean-square (RMS) of the AVISO SSH as a proxy of its surface distribution. Figure 4 displays the time-mean value of EKE from satellite data (Figure 4a) and from our five simulations (Figures 4b–4f), computed by subtracting to its value at each grid point the spatiotemporal average

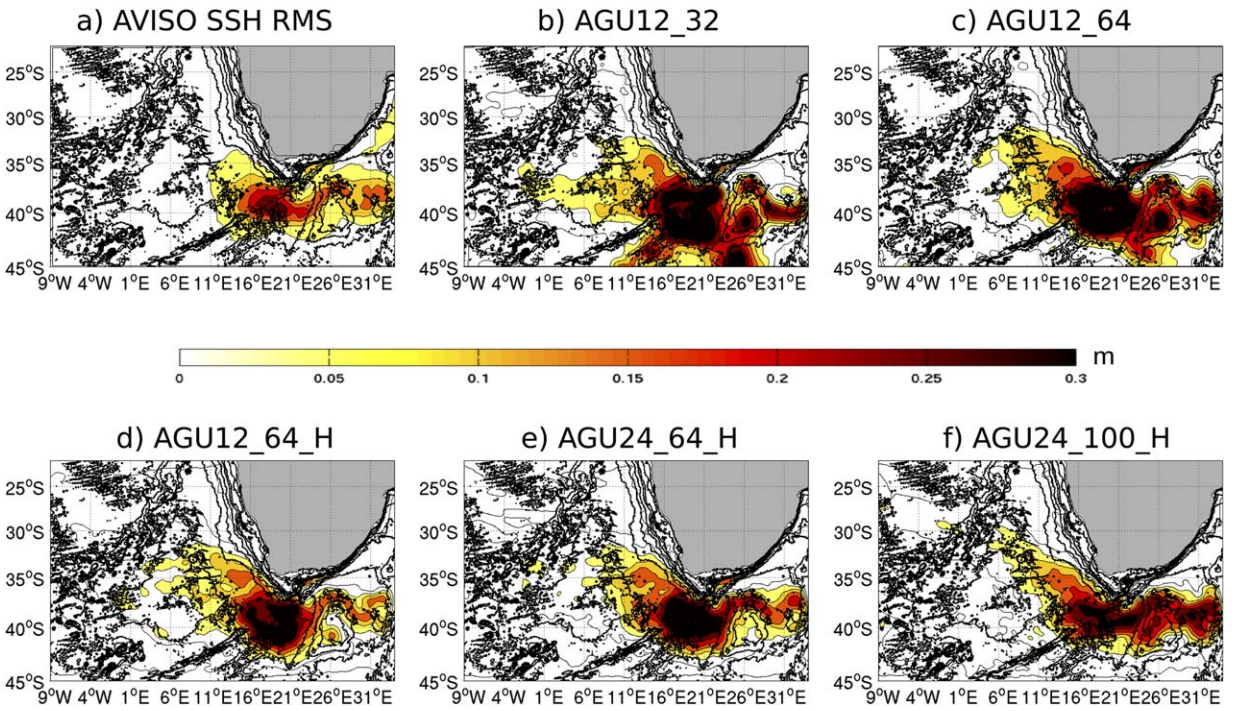

Figure 4. The root-mean-square of the mean Sea Surface Height (m) for (a) the AVISO satellite altimetry gridded product and (b-f) for the model simulations. The bottom topography is shown by the black lines tracing the −5,000, −4,000, −3,000, −2,000, −1,000, −500, −200, −100 m isobaths from the Etopo2 data set (Smith & Sandwell, 1997).

over the whole domain. Both, AVISO and the modeled distributions of SSH RMS show low values (about 0.05–0.1 m) offshore and along the northwestern coast of southern Africa, and high values (0.15–0.3 m) at the Agulhas Retroflection and in the southern Cape Basin (roughly west of 10°E). This corresponds to the intense mesoscale activity driven by Agulhas eddies shed by the Agulhas Current system and found along the South-African continental slope and in the Cape Basin. While the spatial pattern of the modeled EKE agrees well with AVISO, its magnitude is generally higher than the one observed. This bias is greatest near the Agulhas Retroflection and along the shelf downstream; it could be ascribed, on one hand, to the satellites inability to capture nearshore dynamics and to its coarse resolution, preventing the observation of the smallest mesoscale structures. On the other hand, the model bias in EKE could be due to its tendency to overestimate the Agulhas leakage, causing an enhanced horizontal gradient of density structure between the shelf and offshore, and increasing local instabilities near the shelf-edge (Rubio et al., 2009).

The high degree of turbulence in all the simulations extends from the surface down to intermediate layers. Indeed, most eddies have a deep, dynamical influence in the ocean interior. Therefore, changes in their surface structure have been observed to regionally affect also the energetics and thermohaline properties of waters at intermediate depths (Schmid et al., 2003). The snapshots of the vertical component of relative vorticity (ω), computed along the 27.2 isopycnal, reveal the scales that spontaneously develop at the AAIW level (supporting information Figure S3). Every simulation shows the main features of the regional turbulence and its characteristic scales: mesoscale eddies of both signs, meanders and filaments form in all runs, spatially concentrating around the Agulhas Retroflection area, in the Cape Basin and along the main topographic features of the central and south-western parts of the domain. Even though all the simulations show similar patterns of ω, their spatial scales decrease, they become more localized and finer structures are more recurrent, as the model resolution increases both horizontally and vertically. This clearly appears also in Figure 4.

To gain understanding on the level of simulated eddy energy in comparison with observations, we have quantified the Eddy Available Potential Energy ($EAPE = -\frac{g}{2\rho_0}\overline{\zeta'\rho'}$, where ζ' is the isopycnal displacement and ρ' is the associated density anomaly) (Roullet et al., 2014) along the 27.2 isopycnal. Here we have slightly modified the EAPE formulation from the original version of Roullet et al. (2014) by replacing the virtual density with potential

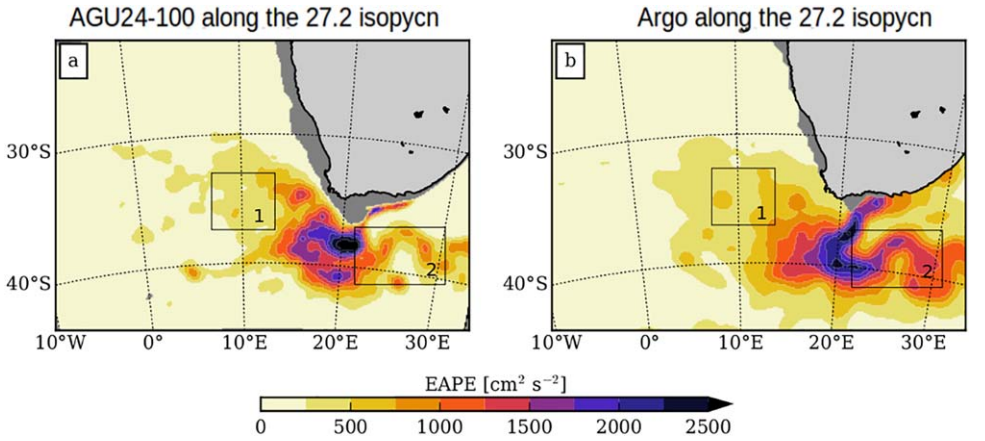

Figure 5. (a) Distributions of the mean Eddy Available Potential Energy (in $cm^2\ s^{-2}$) along the 27.2 isopycnal from (a) the highest resolutions simulation and (b) from Argo data. The black boxes (1 and 2) represent particular areas discussed in the text.

density and including more recent Argo vertical profiles (up to July 2015). EAPE can be considered a proxy of the turbulent state of the ocean interior since its variations are due to the vertical displacement and tilting of the isopycnals (Roullet et al., 2014). The EAPE distribution and magnitude are comparable to those of EKE as, in the quasi-geostrophic framework, an equivalence between EAPE and EKE stems from the hypothesis of 3-D isotropy of developed turbulence (comparable magnitudes of ω and Q) (Roullet et al., 2014). Hence, EAPE can be usefully computed in models and compared to observations in order to validate the energy content of the ocean also at depth, complementing the surface information provided by EKE estimates.

In Figure 5 are presented the 27.2 isopycnal EAPE distributions for (a) the highest resolution simulation (AGU24_100_H), and (b) for Argo data. The modeled EAPE distribution compares relatively well with Argo estimate at the AAIW level, particularly within the region of the Cape Basin (box 1 of Figure 5) and less so east of the Retroflection (box 2 of Figure 5). This difference could be partly due to the absence of synoptic variability in the model boundary conditions (at the surface and lateral boundaries). It could also be explained by the position of the easternmost boundary of the domain, likely positioned too close to the Retroflection area to correctly reproduce the energetics and dynamics of the AC System that depend on the Agulhas upstream mesoscale dynamics (Biastoch et al., 2008). Instead, west of the Retroflection, within the Agulhas rings corridor, the modeled EAPE values and shape better agree with observations, allowing us to validate the energy content of this simulation also at depth and to gather a more quantitative knowledge on the turbulence level characterizing the Cape Basin intermediate layers.

3.5. Mesoscale Eddies Statistics

This subsection aims to statistically describe the geometrical and dynamical characteristics of the simulated eddies. In order to do so, we implemented in our different simulations the eddy-detection algorithm of Pegliasco et al. (2015). This enabled us to estimate the number, sign, size, amplitude, and mean trajectory of all the simulated mesoscale eddies and to compare them to the equivalent estimates from altimetry. It is nowadays known that due to the limited resolution and coarse interpolation processing of the satellite products, these observations are only able to capture the largest mesoscale structures. In fact, as recently shown by Keating and Smith (2015), existing satellite altimetry products struggle to resolve scales within the 10–50 km range and below. Therefore, in order to make our eddy-detection results as comparable as possible to the ones derived from AVISO, we have filtered out all the modeled mesoscale structures whose radius was equal or smaller than 30 km.

Figures 6a–6d show the mean number and radius of the detected anticyclones and cyclones in our simulations after the filtering process (see supporting information Figure S4 for the nonfiltered results), along with the ones from AVISO. Here the normal probability density functions (PDFs) have been fitted to their distributions, which do not substantially differ from the nonfiltered version of these results in terms of simulations intercomparison. The number of detected cyclones is always slightly higher than that of anticyclones (in a

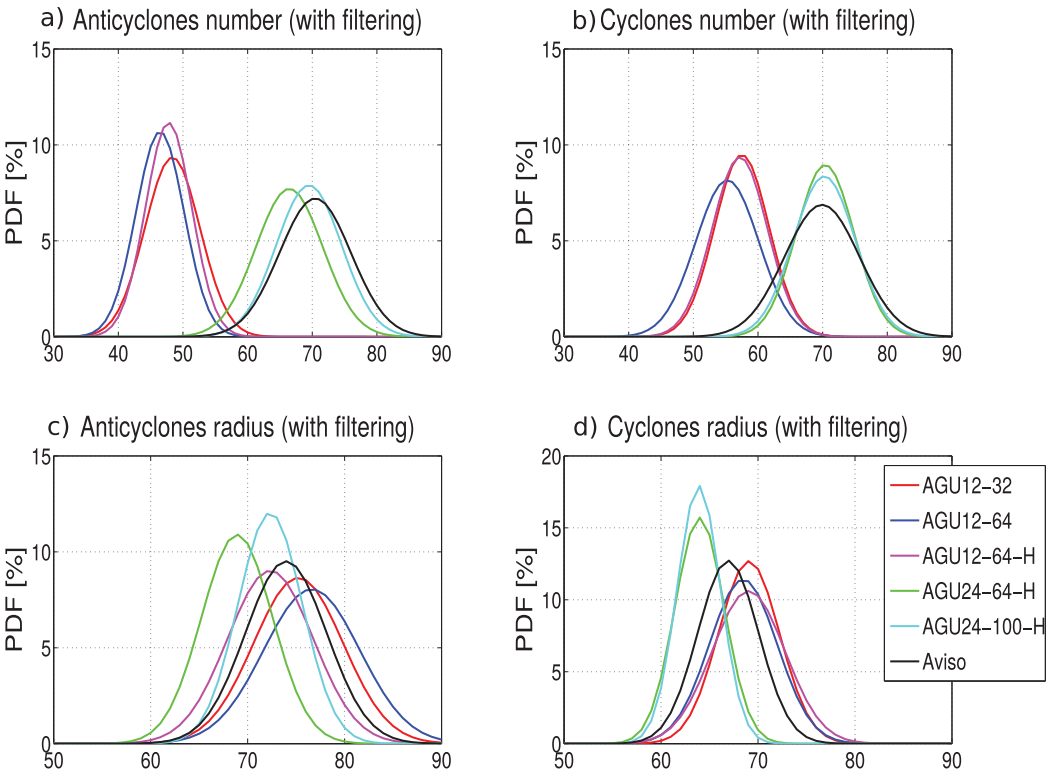

Figure 6. Probability density functions fitted to the time series of the number of (a) anticyclones and (b) cyclones and the mean radius of (c) anticyclones and (d) cyclones detected in each of the five numerical simulations (colored lines) and from AVISO data (black line). Here the modeled eddies whose radius was equal or smaller than 30 km have been filtered out, in order to make them more comparable to the AVISO resolution.

ratio of 3/2, Figures 6a and 6b) for all the simulations, as originally proposed by Boebel et al. (2003) from quasi-Lagrangian observations achieved with deep floats south of Africa. This asymmetry in the eddies number is also suggested from numerical studies of geophysical turbulence in idealized frameworks (Roullet & Klein, 2010). The mean radius is usually larger for the anticyclones than for the cyclones (∼75 versus 65 km, Figures 6c and 6d), as observed in geophysical stratified flows (Lapeyre & Klein, 2006) and for the region of study (Boebel et al., 2003; Richardson & Garzoli, 2003).

Looking at the differences between the unfiltered distributions of the various simulations (supporting information Figure S4), those at the highest resolutions (AGU24_64_H and AGU24_100_H) show the most bountiful presence of eddies, reaching a mean value of 110 for cyclones and 90 for anticyclones, versus mean values of, respectively, 90 and 70 identified in the 1/12° runs. The situation is reversed in terms of their mean radius: smaller values are found for the highest resolution simulations (∼50 km) than for the lowest resolution counterparts (∼60 km).

Once filtered, the results of our highest resolution simulations (AGU24_64_H and AGU24_100_H) agree particularly well with those from altimetry, in terms of the number of both anticyclones and cyclones (Figures 6a and 6b). It is less so for their mean radius (Figures 6c and 6d), as the mesoscale eddies captured in AVISO are slightly larger than those of our 1/24° simulations and are closer to the ones at lower resolution. We believe that this is due to the fact that at finer resolutions eddy baroclinic modes higher than the first two (barotropic and first baroclinic), when properly resolved (as in our 1/24° simulations), enrich the scales and energetics of the first two modes, increasing the presence of smaller structures (Barnier et al., 1991). Another possible explanation would be that when fine horizontal scales are resolved, they can interact among each other and lead to the formation of additional mesoscale structures (Barbosa Aguiar et al., 2013). This phenomenon is obviously missing if these scales are not captured by a limited resolution of the model.

The discrepancy between the number of eddies detected in the nonfiltered distribution of our highest resolution simulation (AGU24_100_H, supporting information Figure S4) and AVISO is evident also in Figure 7,

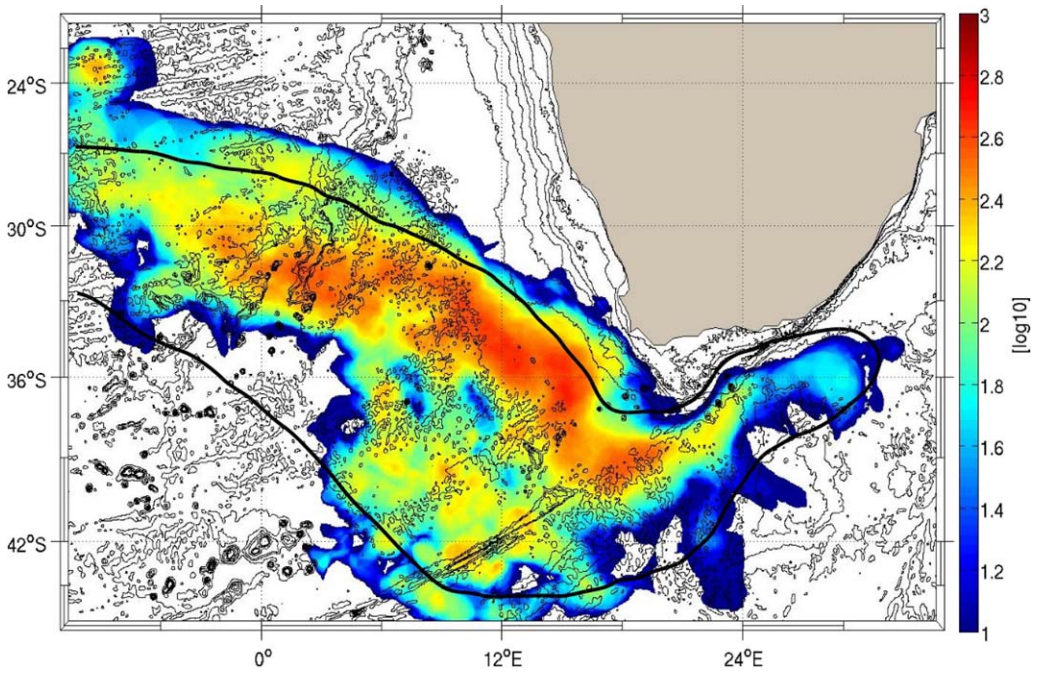

Figure 7. The mean presence of Agulhas Rings, as detected in AGU24_100_H, in color shading and expressed with a logarithmic decimal scale. The thick, black line delimit the same estimate from AVISO. The underneath black contours are for the −5,000, −4,000, −3,000, −2,000, −1,000, −500, −200, −100 m isobaths from the Etopo2 data set (Smith & Sandwell, 1997).

showing the estimates of the mean pathways followed by Agulhas Rings in the Cape Basin from AGU24_100_H and AVISO. Rings are defined in this analysis as anticyclones initially detected in the Southwest Indian sector within a trapezoidal area extending between 12°E–34°E and 34°S–44°S. Here the number of anticyclonic trajectories that are formed or disappear in each grid cell of the model are computed taking into account that a new trajectory starts when a new eddy appears or when an eddy splits into two or more smaller eddies and similarly a trejectory ends when an eddy disappear from the SSH field or when two eddies merge. The colored cloud of AGU24_100_H in Figure 7, representing the mean percentage of rings per grid-box along their trajectories, is slightly shifted north-westward compared to the AVISO envelope represented with a black contour.

This difference in the directions of Agulhas Rings mean path could be explained by: (1) smaller or more intense simulated rings than those detected in AVISO, and thus anticyclones less sensitive to the β-effect; (2) a (westward) shift in the position of the simulated Agulhas Retroflection, where the process of rings shedding is known to take place; (3) an enhancement in the intensity or a more northward location of the simulated subtropical gyre than in observations, leading to an advection of more rings northward; (4) a discrepancy either in the vertical size of the rings or in their intensity at depth, resulting in a different bathymetric deflection. In this study, the first condition was verified: the anticyclones surface signature in EKE was shown to be higher than what observed in the altimetric product (Figure 5) and their radius is averagely smaller than the rings detected in AVISO (Figure 7c). The second condition was also partially verified by running some sensitivity tests (not shown), where the eastern boundary of our simulated domain was placed slightly more westward than presently (30°E instead of 34°E), inducing a substantial reduction in the mean EKE content of the test runs. We expect that placing this boundary even further east then 34°E, although highly augmenting the computational costs of the run, would allow us to reproduce a more realistic Agulhas Retroflection. An even larger domain and a longer simulation would be required to test the third condition on the subtropical gyre position and intensity, whereas a three-dimensional reconstruction of the eddies from AVISO would be necessary to investigate the fourth condition.

In general, the displacement of coherent mesoscale structures in the ocean is attributed, in addition to the influence of the β-effect and of topography, also to the influences of neighboring currents and to the interactions with other eddies, which account for the loops and cusps in their trajectories (Carton, 2001). Since

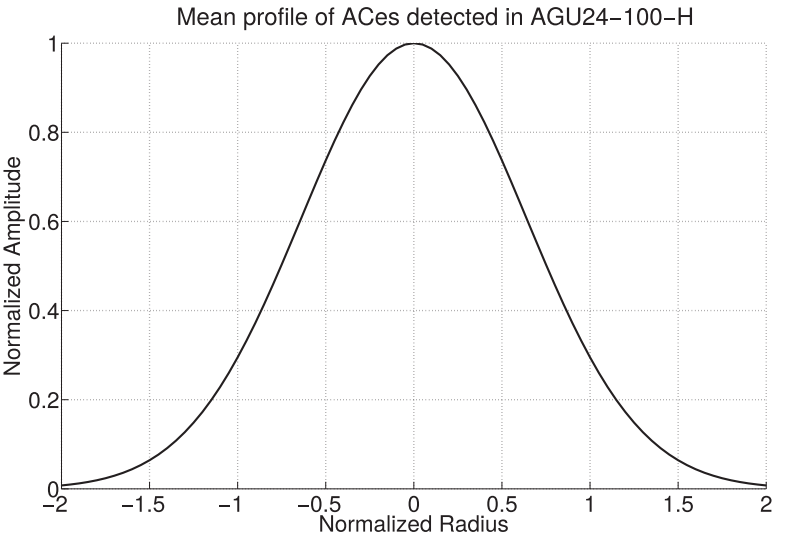

Figure 8. Mean profile of the anticyclones detected in AGU24_100_H, plotted as their mean amplitude, normalized by their mean number, against their normalized radius.

the Cape Basin is characterized by the coexistence of cyclonic and anticyclonic vortices, generated in proximity of the continental slope and at the Agulhas Retroflection, eddy merging and splitting events, as well as absorption and detachment from the main current, are expected to highly impact the Agulhas rings trajectories and also their geometry. Therefore, we statistically examined their two-dimensional structure, by tracing their mean amplitude, normalized by their mean number, against their normalized radius. Figure 8 shows that the anticyclones mean profile (given by the mean SSH eddy amplitude versus the eddy radius) in AGU24_100_H has a quasi-Gaussian shape, in line with previous results on global scale (Chelton et al., 2011). Since investigating the relation between the eddy horizontal geometry and the different mechanisms of eddy deformation goes beyond the scopes of this paper, in the following we will only examine the temporal variability of the simulated eddies and its driving factors.

3.6. Temporal Variability of the Mesoscale Dynamics

The monthly time series of the number of eddies detected in each numerical experiment (not shown here), from which we computed the eddy-PDF distributions of Figure 6, disclose a temporal-dependent behavior. In particular, these time series are characterized by a strong seasonal cycle, more pronounced for the higher resolutions simulations (AGU24_64_H and AGU24_100_H).

This seasonality could be further investigated through the analysis of a longer simulation in order to test its statistical significance over a more extended time series. However, in order to ascertain this seasonal variability with observations, we plotted the mean monthly time series of the number of eddies detected from AVISO and for our highest resolution simulation (Figure 9) and we undertook preliminary analyses to investigate possible processes responsible of such variations. We observe that in both time series the seasonal cycle is distinguishable (Figures 9a and 9b); it is particularly marked in the model distribution, where the winter maximum (July–September) clearly appears for eddies of both polarities. This temporal variability was further explored, performing a discrete Fourier transform on these two time series (Figures 9c and 9d); it suggests that an annual cycle is dominant for both observed and modeled eddies.

Multiple factors could be responsible of this time-dependence of the mesoscale field. Among these are the variability of the atmospheric forcing, the seasonality of the regional upwelling or the local influence of intermittent Natal Pulses (de Ruijter et al., 1999; Schouten et al., 2003; van Leeuwen & de Ruijter, 2000). Given that the surface forcings and boundary conditions of our simulations are based on interannual, smoothed climatologies, our simulations do not allow us to explore these factors. But, we can analyze three oceanic metrics that relate mesoscale eddies to their generation processes: the EPV (Marchesiello et al., 2003; Peliz et al., 2014); the first baroclinic Rossby radius of deformation (computed along the pycnocline, as in Chelton et al., 1998), relating the eddies size and temporal distribution to their formation mechanism

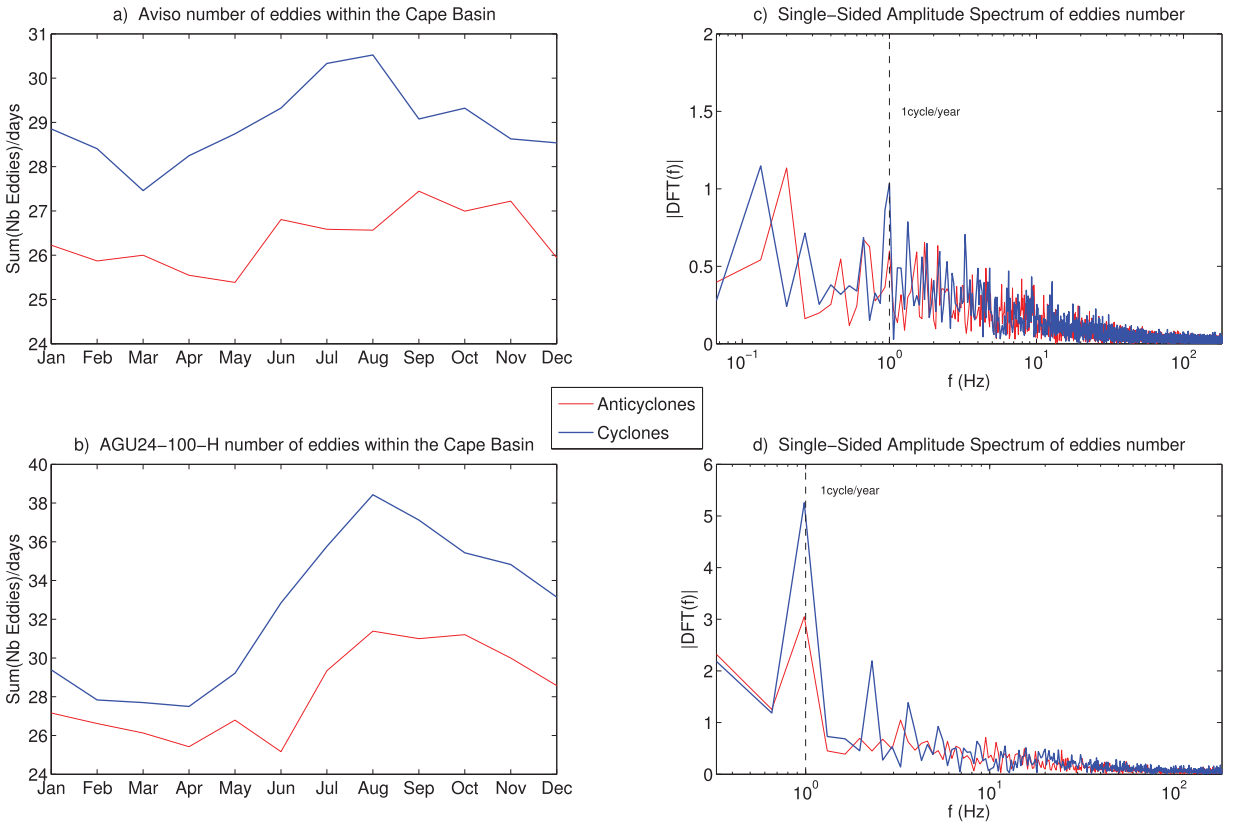

Figure 9. Seasonal time series of the mean number of anticyclones (red) and cyclones (blue) for (a) AVISO and (b) AGU24_100_H. Single-Sided Amplitude Spectrum from the discrete Fourier transform of these distributions for (c) AVISO and (d) AGU24_100_H.

(Chelton et al., 2011; Smith, 2007); and the mixed-layer depth (MLD, calculated as the depth where the density difference with respect to the surface is equivalent to a 0.03 density change), whose seasonality, in relation to that of eddy dynamics, has been recently explained as linked to meso-submesoscale interactions (Brannigan, 2016; Callies et al., 2015).

In this framework, we will consider the EPV anomaly (EPVA), quantifying the EPV difference with the background ocean, and its vertical components (i.e., the first RHS term of equation (1)). These terms, as well as the Rossby radius and the MLD, are averaged over the geographical domain during the last year of each simulation (year 5). The results are presented for AGU12_64 and AGU24_100_H. Figure 10a shows the time series of the EPVA, obtained by subtracting from each instantaneous value of EPV the interannual mean over the last 3 years of integration (this was the period we used for the eddy detection in our simulations). Figure 10b displays the EPV vertical components (i.e., the relative vorticity and the vortex stretching terms). The EPVA for the highest resolution simulation (AGU24_100_H, black continuous line in Figure 10a) is characterized by a marked seasonality, in which negative and positive values alternate, reaching a maximum during the austral winter. This maximum corresponds to those of the vortex stretching and relative vorticity terms (respectively, blue and red continuous lines in Figure 10b). The vortex stretching is directly linked to the stratification, which is indeed higher in summer as a consequence of the seasonal warming, and declines in winter by cooling and under the action of stronger winds. These conditions favor higher values in the temporal distribution of relative vorticity (red, continuous line in Figure 10b) in winter, when more ageostrophic, turbulent dynamics are at play, increasing the seasonal values of the EPV anomaly.

A clear seasonality is also distinguishable in the time series of the first baroclinic Rossby radius of deformation and in that of the MLD (Figure 10c) for both model resolutions (AGU12_64 and AGU24_100_H, respectively, dashed and continuous lines in Figure 10c). Because the first Rossby radius is associated to the fastest growing mode for the baroclinic instability (Rhines, 1975), its winter maximum corresponds to a seasonal peak in the time series of the mean eddy radius. We can retrieve these winter peaks in the 3 years time series of the mean radius of both cyclones and anticyclones (not shown here). These peaks are well

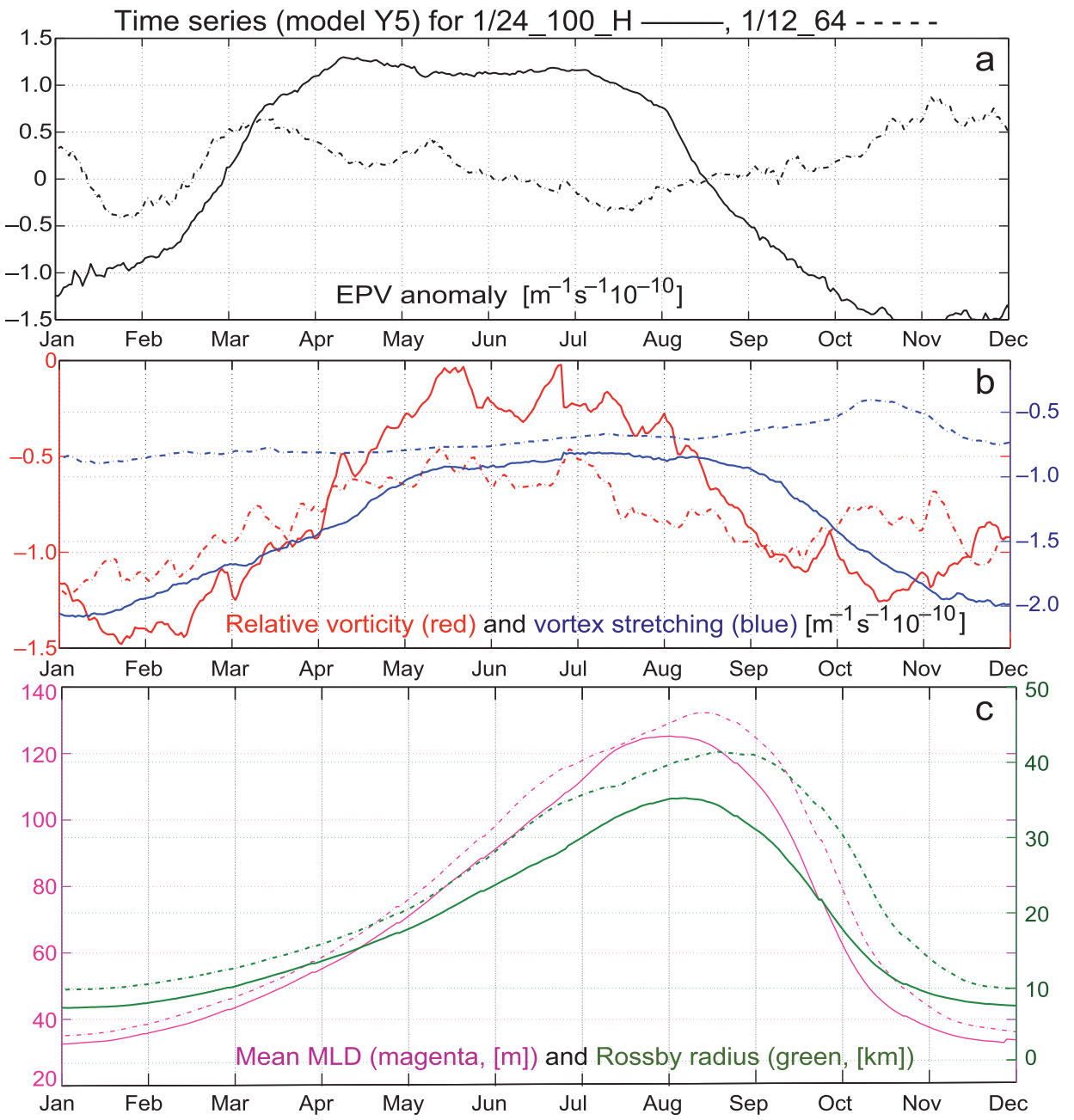

Figure 10. Time series of the surface spatially averaged (a) Ertel PV anomaly, (b) its vertical components, (c) Rossby radius and mixed-layer depth, for AGU12_64 (dashed lines) and AGU24_100_H (continuous lines).

marked in the higher resolution simulations (AGU24_64_H and AGU24_100_H); this confirms the relationship existing between the eddy size and the local Rossby radius of deformation, suggested by several studies (Aubert et al., 2012; Carton, 2001; McWilliams, 1991). Indeed, upper-ocean eddies often form from the development of baroclinic instability, essentially projecting on the barotropic and on the first baroclinic modes. Consequently, their size is close to the first baroclinic Rossby radius of deformation. A winter increase of the eddies mean radius also occurs in the lower resolution simulations (not shown), corresponding to the winter peak of the Rossby radius of deformation (dashed line in Figure 10c, displaying these values for AGU12_64).

On the other hand, the time series of the EPV anomaly for AGU12_64 (black, dashed line in Figure 10a), does not show a well-defined seasonal cycle, in relation with limited seasonal variation of the vortex

stretching term (blue, dashed line in Figure 10b). This suggests that the lower resolution simulations (at 1/12°) are not able to correctly reproduce the seasonal cycle of baroclinic instabilities. Indeed, while they capture the seasonal evolution of relative vorticity (red, dashed line in Figure 10b), driven by the largest mesoscale structures, they cannot recover the variability in the vortex stretching, highly affected by finer scales dynamics (Brannigan, 2016; Callies et al., 2015; Capuano et al., 2018).

To conclude this subsection on eddy seasonality, we estimate its impact on thermohaline fluxes, computing the diffusion coefficients of temperature and salinity, Kv_T and Kv_S, defined as in Joyce (1977):

$$<w'T'> = Kv\_T\frac{\partial \bar{T}}{\partial z},$$

$$<w'S'> = Kv\_S\frac{\partial \bar{S}}{\partial z},$$

where w is the vertical velocity; brackets and prime, respectively, denote a time average and fluctuations relative to it, and the bar represents a spatiotemporal mean.

The strongest heat and salt fluxes coincide with the presence of eddies of both polarities, with a clear seasonality. Their summer distribution (not shown here) is characterized by enhanced values of these fluxes in correspondence of the largest mesoscale structures, while in winter we observe an abundance of finer scales, locally leading to higher values for both diffusion coefficients. To better quantify this seasonality we computed the horizontal spectra of the diffusivities (Figure 11) at the surface and along the 27.2 isopycnal in the Cape Basin box of Figure 1, during summer and winter. At the surface, the seasonal contrast is very pronounced at small scales, which present similar values of diffusivity as the larger scales. Instead, at depth, the seasonal difference does not seem to depend on the horizontal scales; also here we observe a winter increase in the values of diffusivities. These processes have been investigated in more detail in Capuano et al. (2018) where it has been suggested that submesoscale instabilities of the mesoscale field play a role on the vertical thermohaline structure of the local water masses. Such processes are partially represented by AGU24_100_H.

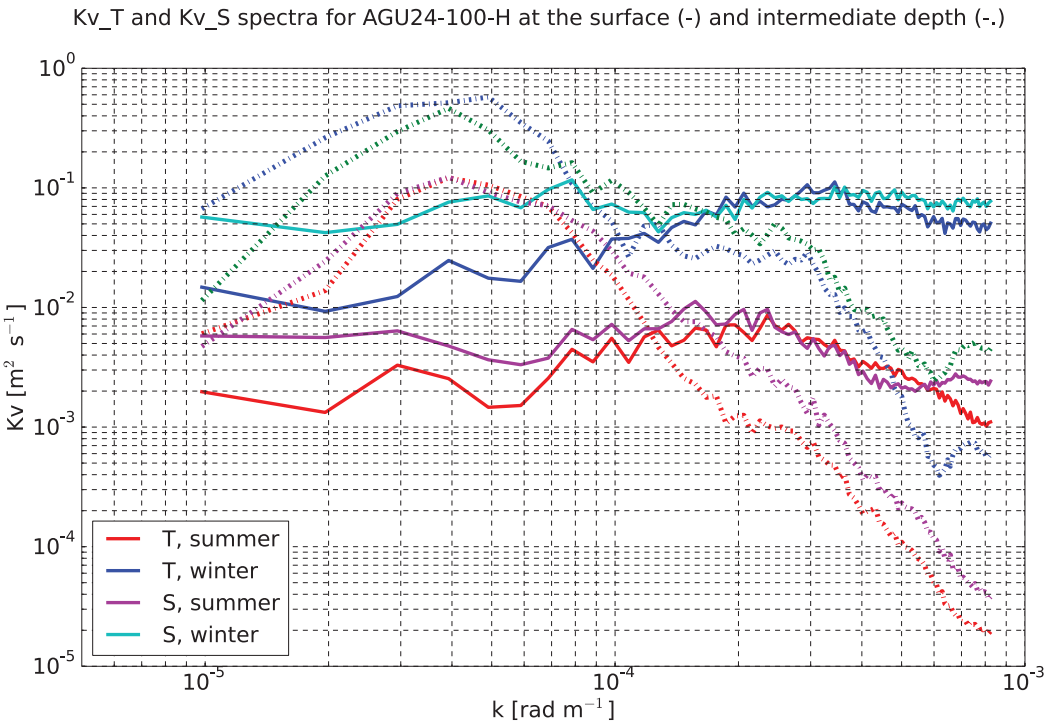

Figure 11. Horizontal spectra of the diffusion coefficients of temperature and salinity, computed for AGU24_100_H at the surface (continuous lines) and at intermediate depth (dashed lines) in summer and winter.

3.7. Eddies Signature on AAIW Advection

Since this work is centered on the impact of the mesoscale dynamics on the Indo-Atlantic exchange and regional mixing of AAIW, we focus here on the properties of water masses advected in the Cape Basin by the simulated mesoscale features. To assess subsurface water mass properties within the eddies, we have estimated the θ–S diagram corresponding to the center of every eddy detected in each simulation within the Cape Basin box lying on the principal route of the Agulhas leakage (box drawn in Figure 1). All these θ–S profiles are shown for every simulation for anticyclones in Figure 12a, and for cyclones in Figure 12b.

These diagrams illustrate how the vertical thermohaline properties in the AAIW layer of the eddies change with the model resolutions. At lower vertical and horizontal resolutions, the eddy-core AAIW θ-S properties diverge from those of Argo profiles (light green dots in Figures 12c and 12d). AAIW as measured by Argo floats is fresher than that advected within the simulated eddies, with the exception of the highest resolution simulation (AGU24_100_H) that well compares with the observations (light blue dots in Figures 11a and 11b, and red and blue dots in Figures 12c and 12d). Thus, advection and mixing of water masses in the Cape Basin, and in particular within the AAIW layer, are represented in models with a horizontal resolution of 1/24° and a vertical resolution of about 50 m or higher.

However, despite the differences in AAIW properties within the core of eddies among the various simulations and in comparison to Argo data, it appears that these properties are, in the Cape Basin, relatively homogeneous. Both cyclones and anticyclones show indeed salinities values in the AAIW layer ranging from 34.25 and 34.4 psu (in the AGU24_100_H simulation) in accordance with the Argo sampled properties and with historical hydrographic cruises (Arhan et al., 2012; Giulivi & Gordon, 2006; Richardson & Garzoli, 2003). This implies that both types of eddies are involved in the advection of the same AAIW varieties, namely the Indian (I-AAIW: $S \geq 34.3$) and the Indo-Atlantic (IA-AAIW: $34.2 < S < 34.3$) ones (Rusciano et al., 2012). This is also in agreement with the findings of Arhan et al. (2011) from in situ observations of an Agulhas Ring and an Agulhas Bank cyclone in the southern Cape Basin, along the GoodHope line. Thus, in line with the results of Rimaud et al. (2012), cyclones are as fundamental as anticyclones for the transport, mixing, and transformation of I-AAIW with AAIW of Atlantic origin ($S \leq 34.2$) within the Cape Basin, before entering the South Atlantic (Figure 12).

The significant improvement that we gained, with the highest resolutions simulation, in the reproduction of the modeled thermohaline structure is reflected also in the interocean exchange of upper and lower thermocline waters. Here we used the offline mass-preserving algorithm ARIANE (Blanke et al., 1999; Blanke & Raynaud, 1997) to perform in each simulation a Lagrangian integration, backward in time, of particles selected as those having density values (25–27.6σ) typical of thermocline waters in the Cape Basin. These particles were initialized at the east section (in red) and intercepted at the north and western sections (in black) of the control domain shown in the map of Figure 13b, where the colored curves represent the transport stream function (PSI). The latter is estimated in the model simulations by algebrically summing every particle transport at each velocity point of the three-dimensional grid, before vertical integration and derivation of the Lagrangian stream function, showing a max value of 8 Sv (1 Sv $= 10^6$ m^3 s^{-1}) in AGU24_100_H. This value is comparable with previous estimates of the Indo-Atlantic transfer (9 Sv of Boebel et al., 2003), 12 SV of Biastoch et al. (2008).

We then plotted the histogram bars of the difference between the final and the initial transports, computed as the number of particles normalized by their total transport and binned by potential density classes (Figure 13a) for AGU12_32 (red), AGU12_64_H (magenta), and AGU24_100_H (cyan). For this calculation, the potential density changes are estimated between successive positions (archived everyday) and by algebraically summing the individual and local density changes weighted by the transports allotted to the corresponding particles. The spatial integration of this field is roughly equal to the magnitude of the transfer multiplied by the mean difference in density between the final and initial sections. This diagnostic allowed us to verify that the highest resolutions simulation is the only one able to correctly capture the transport, from the Indian to the Atlantic oceans, of thermocline waters, consisting of the lighter variety of mode and intermediate waters (highlighted, respectively, in green and blue in Figure 13a). The model inability, at lower resolution, to capture a part of the local mesoscale processes implies a prominent reduction in the quantity of transport of thermocline waters from the Indian to the Atlantic oceans. These preliminary results indicate that the Cape Basin turbulent dynamics have a direct effect on the characteristics and transfer of the water masses participating in the AMOC, and confirm that this region is essential in connecting the ocean basins and making possible a global circulation (Garzoli & Matano, 2011).

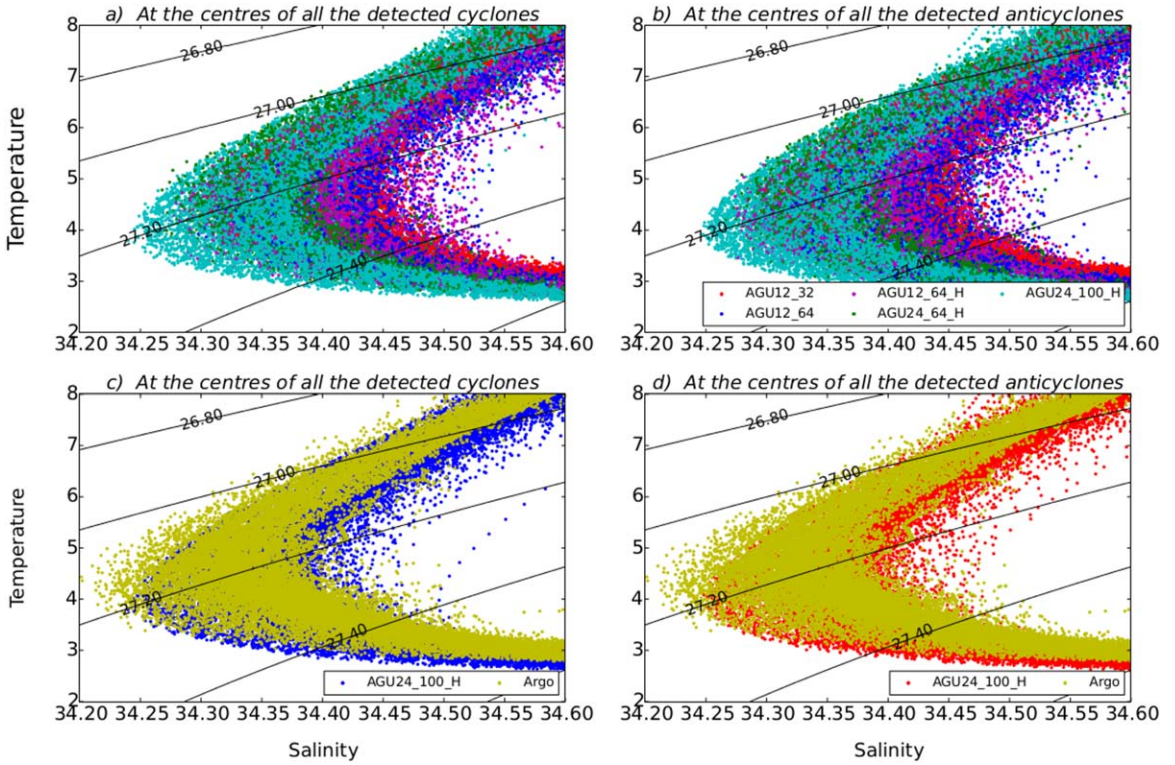

Figure 12. θ–S diagrams plotted at the center of all the anticyclones (a) and of all the cyclones (b) detected in each of our five simulations for the AAIW thermohaline range (8–2°C of θ and 34.2–34.6 psu of S). (c and d) Identical to a and b, except the comparison is between the θ–S distribution of AGU24_100_H and Argo.

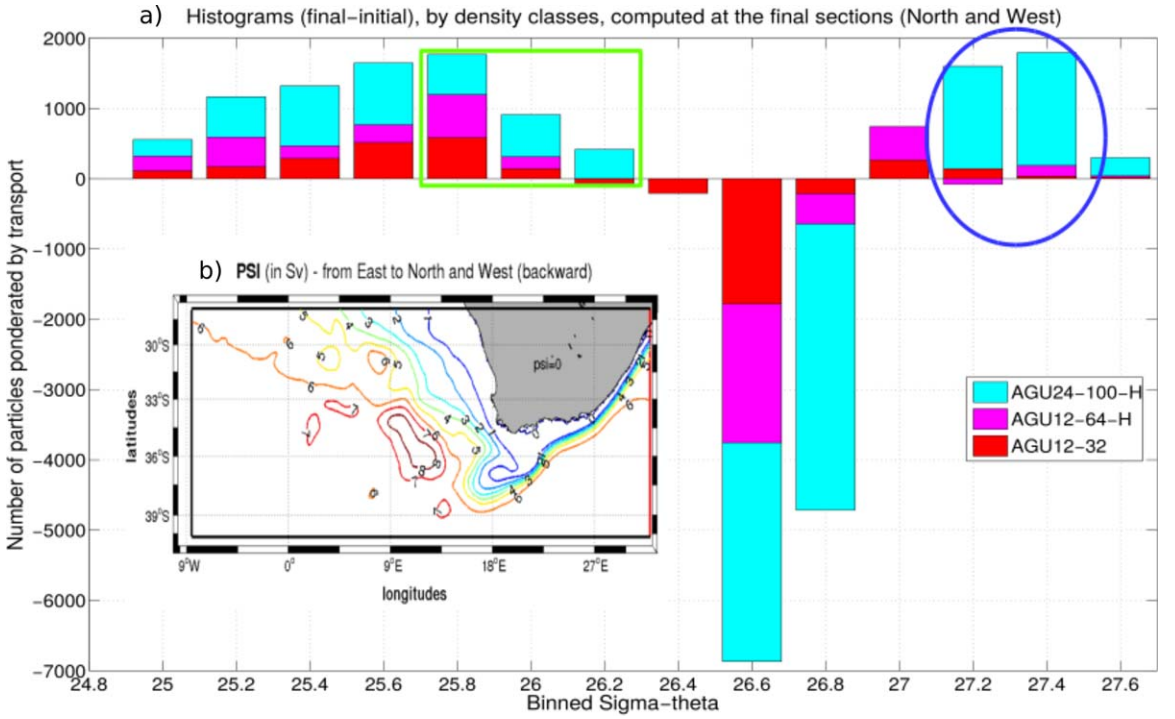

Figure 13. (a) Histograms of the differences between the final and initial Lagrangian transports [Sv], binned by density classes, for AGU12_32 (red), AGU12_64_H (magenta), and AGU24_100_H (cyan), computed within the domain control shown in the transport stream function map (b). In Figure 13a, highlighted in green are the lighter varieties of mode waters and in blue the Atlantic and Indo-Atlantic varieties of AAIWs.

4. Summary and Conclusions

The Indo-Atlantic exchange of thermocline waters south of Africa strongly depends on highly energetic mechanisms, affecting subsurface water masses advection and mixing. By improving the simulation of the nonlinear dynamics that drives this exchange, we were able to capture a realistic part of the ocean mesoscale processes that transport and stir the local water masses. In particular, we demonstrate how a satisfactory representation of the surface dynamics is not sufficient to ensure a realistic upper and intermediate water masses advection and transformation. We obtained the most prominent improvements in simulating these processes by augmenting and homogenizing the vertical resolution of the model to reach a 50 m spacing between the levels. This increase in the vertical resolution of the water column positively impacts also the surface ocean dynamics. A doubling of the horizontal grid-spacing (from 8 km in the 1/12° to 4 km for the 1/24°) improves even further the realism of the simulations.

By increasing the model resolution both vertically and horizontally, we show that:

1. The contrast between the southwest Indian and the southeast Atlantic waters becomes sharper, with distinct structures of the thermocline as it is observed in the real ocean. Water masses in the subsurface layers compare particularly well to observations from classical hydrography and Argo profiles.
2. In finer resolutions simulations mesoscale dynamics and energetics are generally in better agreement with the available observations. The highest resolutions configuration clearly shows a dynamical behavior change, with a richer spectrum of spatiotemporal scales and more nonlinear processes than classical eddy-permitting (at 1/12°) simulations. This appear clearly in the diffusivities spectra, where smaller length scales are reached, both at the surface and at depth.
3. A precise estimate of the distribution, size, and properties of the simulated upper-ocean eddies of both signs can be achieved by applying the detection algorithm of Pegliasco et al. (2015) to the output of each of our simulations. Remarkably all the runs are characterized by an asymmetry among cyclones and anticyclones, the former being always more abundant (in a ratio of 3/2) and smaller in radius (about 65 versus 75 km), as already suggested in previous, observational and theoretical, studies.
4. The structure and mean pathways of the modeled Agulhas rings compare well with their counterparts estimated from altimetry, once the simulated eddies having radius equal or higher than 30 km are filtered out. Considering the limitations in the resolution of the satellite products, results of the 1/24° simulations better agree with these data after the filtering process, even though a slight discrepancy persists in terms of the mean radius. However, in AGU24_100_H, Indian-water anticyclones can be clearly retrieved within the migration drift path of the observed Agulhas Rings into the South Atlantic (Boebel et al., 2003; Dencausse et al., 2010).
5. Both types of eddies, cyclones and anticyclones, contain the Indian variety of AAIW (I-AAIW) as suggested by Richardson and Garzoli (2003), Giulivi and Gordon (2006), and Arhan et al. (2011) from sparse hydrographic observations. We also corroborate the finding that in the Cape Basin, the eddies advecting I-AAIW experiences mixing with the Atlantic variety of AAIW (A-AAIW) producing a new variety, the Indo-Atlantic AAIW (IA-AAIW), whose properties are intermediate between the two AAIWs, as discussed by Rusciano et al. (2012) and Rimaud et al. (2012).
6. The number and radius of eddies (of both signs) show a seasonal cycle. The latter is largest for the highest resolutions simulations displaying a maximum in the eddies number and radius during winter, when the first baroclinic Rossby radius of deformation is also maximum. This supports baroclinic processes as key mechanisms for the generation of these eddies, while undoubtedly linked with the seasonality of the EPV anomaly, of its vertical components and with the one of the MLD.
7. The diagnostic tool ARIANE provided a Lagrangian interpretation of the modeled Indo-Atlantic exchange. This allowed us to quantify the intensity of thermocline waters transfers and mixing, and to illustrate that at least a fully mesoscale-resolving resolution of the model is required to depict the Cape Basin dynamics and transformations inherent to these transfers.
8. The last two points underline the need for numerical experiments at higher horizontal resolution than 1/24°, which would allow the representation of an even broader range of scales (including submesocale filaments, fronts, meanders), whose spatiotemporal variability could explain the seasonal correlation between the eddy statistics and the dynamical metrics obtained here. Also, we expect the use of synoptic surface forcing and more realistic boundary conditions, in a fully submesoscale-resolving configuration, to further improve the reproduction of the flow instabilities seasonality and their effect on the thermohaline properties and spreading of the Indo-Atlantic waters into the AMOC.

The challenges presented by high-resolution requirements to solve the realism of the ocean circulation will accompany global ocean modeling efforts. In this respect, ocean models must have consistently high resolution, both horizontally and vertically, and particular attention must be paid to correctly simulate the baroclinic structure of the subsurface and deep water masses.

Acknowledgments
The model data used analyzed in this paper are available at the following http://data.umr-lops.fr/pub/AGU_MESO/. The authors greatly appreciate discussions with Xavier Capet, Gildas Cambon, Guillaume Lapeyre, Guillaume Roullet, Bernard Barnier, Arne Biastoch, and Jeroen Molemaker. This work was supported by the "Laboratoire dExcellence" LabexMER (ANR-10-LABX-19), by a grant from the French Ministry of Higher Education and Research under the program "Investissements dAvenir," and by a grant from the Regional Council of Brittany. This work was also supported by the European Union Horizon 2020 research and innovation program under grant 633211 (AtlantOS), and by the 11-ANR-56-004 SAMOC research grant. This study is part of the CLIVAR-SAMOC international initiative. We also acknowledge funding from the ANR/DGA program DYNED ATLAS and the French CNRS computer center IDRIS for technical and computational support. The altimeter products were produced by Ssalto/Duacs and distributed by AVISO, with support from CNES. We thank both reviewers who helped us to improve this manuscript.

References

Arhan, M., Speich, S., Messager, C., Dencausse, G., Fine, R., & Boye, M. (2011). Anticyclonic and cyclonic eddies of subtropical origin in the subantarctic zone south of Africa. *Journal of Geophysical Research*, *116*, C11004. https://doi.org/10.1029/2011JC007140

Aubert, O., Le Bars, M., Le Gal, P., & Marcus, P. S. (2012). The universal aspect ratio of vortices in rotating stratified flows: Experiments and observations. *Journal of Fluid Mechanics*, *706*, 34–45. https://doi.org/10.1017/jfm.2012.176

Barbosa Aguiar, A. C., Peliz, A., & Carton, X. (2013). A census of meddies in a long-term high-resolution simulation. *Progress in Oceanography*, *116*, 80–94.

Barnier, B., Le Provost, C., & Hua, B. L. (1991). On the catalytic role of high baroclinic modes in eddy-driven large-scale circulations. *Journal of Physical Oceanography*, *21*, 976–997. https://doi.org/10.1175/1520-0485(1991)021<0976:OTCROH>2.0.CO;2

Biastoch, A., Boning, C. W., & Lutjeharms, J. R. E. (2008). Agulhas leakage dynamics affects decadal variability in Atlantic overturning circulation. *Nature*, *456*, 489– 492. https://doi.org/10.1038/nature07426

Biastoch, A., Lutjeharms, J. R. E., Bning, C. W., & Scheinert, M. (2008). Mesoscale perturbations control inter-ocean exchange south of Africa. *Geophysical Research Letters*, *35*, L20602. https://doi.org/10.1029/2008GL035132

Blanke, B., Arhan, M., Madec, G., & Roche, S. (1999). Warm water paths in the Equatorial Atlantic as diagnosed with a general circulation model. *Journal of Physical Oceanography*, *29*, 2753–2768. https://doi.org/10.1175/1520-0485(1999)029<2753:WWPITE>2.0.CO;2

Blanke, B., & Raynaud, S. (1997). Kinematics of the Pacific equatorial undercurrent: An Eulerian and Lagrangian approach from GCM results. *Journal of Physical Oceanography*, *27*, 1038–1053. https://doi.org/10.1175/1520-0485(1997)027<1038:KOTPEU>2.0.CO;2

Boebel, O., Lutjeharms, J. R. E., Schmid, C., Zenk, C., Rossby, T., & Barron, C. (2003). The Cape Cauldron: A regime of turbulent inter-ocean exchange. *Deep Sea Research, Part I*, *50*, 57–86. https://doi.org/10.1016/S0967-0645(02)00379-X

Brannigan, L. (2016). Intense submesoscale upwelling in anticyclonic eddies. *Geophysical Research Letters*, *43*, 3360–3369. https://doi.org/10.1002/2016GL067926

Bryden, H. L., & Beal, L. M. (2001). Role of the Agulhas Current in the Indian Ocean circulation and associated heat and freshwater fluxes. *Deep Sea Research, Part I*, *48*, 1821–1845.

Callies, J., Ferrari, R., Klymak, J. M., & Gula, J. (2015). Seasonality in submesoscale turbulence. *Nature Communications*, *6*, 6862. https://doi.org/10.1038/ncomms7862

Capet, X., McWilliams, J. C., Molemaker, M. J., & Shchepetkin, A. F. (2008). Mesoscale to submesoscale transition in the California Current System. Part I: Flow structure, eddy flux, and observational tests. *Journal of Physical Oceanography*, *38*, 29–43.

Capuano, T. A., Speich, S., Carton, X., & Blanke, B. (2018). Mesoscale and submesoscale processes in the Southeast Atlantic and their impact on the regional thermohaline structure. *Journal of Geophysical Research: Oceans*, *123*. https://doi.org/10.1002/2017JC013396

Carton, X. (2001). Hydrodynamical modeling of oceanic vortices. *Surveys in Geophysics*, *22*(3), 179–263.

Chaigneau, A., Gizolme, A., & Grados, C. (2008). Mesoscale eddies off Peru in altimeter records: Identification algorithms and eddy spatio-temporal patterns. *Progress in Oceanography*, *79*(2), 106–119.

Chaigneau, A., Marie, L. T., Grard, E., Carmen, G., & Oscar, P. (2011). Vertical structure of mesoscale eddies in the eastern South Pacific Ocean: A composite analysis from altimetry and argo profiling floats. *Journal of Geophysical Research*, *116*, C11025. https://doi.org/10.1029/2011JC007134

Chelton, D. B., deSzoeke, R. A., Schlax, M. G., Naggar, K. E., & Siwertz, N. (1998). Geographical variability of the first-baroclinic Rossby radius of deformation. *Journal of Physical Oceanography*, *28*, 433– 460.

Chelton, D. B., Schlax, M. G., & Samelson, R. M. (2011). Global observations of non-linear mesoscale eddies. *Progress in Oceanography*, *91*(2), 167–216.

Da Silva, A. M., Young-Molling, C. C., & Levitus, S. (1994). *Atlas of surface marine data 1994, vol. 1. Algorithms and procedures* (NOAA Atlas NESDIS 6). Silver Spring, MD: NOAA.

Dencausse, G., Arhan, M., & Speich, S. (2010). Routes of Agulhas rings in the southeastern Cape Basin. *Deep Sea Research, Part I*, *57*, 1406–1421. https://doi.org/10.1016/j.dsr.2010.07.008

de Ruijter, W. P. M., van Leeuwen, P. J., & Lutjeharms, J. R. E. (1999). Generation and evolution of Natal Pulses: Solitary meanders in the Agulhas Current. *Journal Physical Oceanography*, *29*, 3043–3055.

Duacs/AVISO (2014). *A new version of ssalto/duacs products available in April 2014. version 1.1*. France: CNES. Retrieved from http://www.aviso.altimetry.fr/fileadmin/documents/data/duacs/Duacs2014.pdf

Ducet, N., Le Traon, P.-Y., & Reverdin, G. (2000). Global high resolution mapping of ocean circulation from TOPEX/Poseidon and ERS-1 and −2. *Journal of Geophysical Research*, *105*, 19477–19498.

Ertel, H. (1942). Ein neuer hydrodynamischer Erhaltungssatz. *Naturwiss*, *30*, 543–544.

Garzoli, S. L., & Matano, R. (2011). The South Atlantic and the Atlantic meridional overturning circulation. *Deep Sea Research, Part II*, *58*(1718), 1837–1847. https://doi.org/10.1016/j.dsr2.2010.10.063

Giulivi, C. F., & Gordon, A. L. (2006). Isopycnal displacements within the Cape Basin thermocline as revealed by the Hydrographic Data Archive. *Deep Sea Research, Part I*, *53*(8), 1285–1300.

Gordon, A. L. (2001). Interocean exchange. In Siedler, G. et al. (Eds.), *Ocean circulation and climate: observing and modelling the global ocean* (Vol. 77, pp. 303–314). Amsterdam: Academic press, International Geophysics Series.

Gordon, A. L., Weiss, R. F., Smethie, W. M. Jr., & Warner, M. J. (1992). Thermo-cline and intermediate water communication between the South Atlantic and Indian Oceans. *Journal of Geophysical Research*, *97*, 7223–7240. https://doi.org/10.1029/92JC00485

Joyce, T. M. (1977). A note on the lateral mixing of water masses. *Journal of Physical Oceanography*, *7*, 626–629. https://doi.org/10.1175/1520-0485(1977)007<0626:ANOTLM>2.0.CO;2

Keating, S. R., & Smith, K. S. (2015). Upper ocean flow statistics estimated from superresolved sea-surface temperature images. *Journal of Geophysical Research: Oceans*, *120*, 1197–1214. https://doi.org/10.1002/2014JC010357

Lapeyre, G., & Klein, P. (2006). Impact of the small-scale elongated filaments on the oceanic vertical pump. *Journal of Marine Research*, *64*, 835–851.

Lemarie, F., Kurian, J., Shchepetkin, A. F., Molemaker, M. J., Colas, F., & McWilliams, J. C. (2012). Are there inescapable issues prohibiting the use of terrain-following coordinates in climate models?. *Ocean Modelling*, *42*, 57–79. https://doi.org/10.1016/j.ocemod.2011.11.007
Levy, M., Klein, P., Trguier, A.-M., Iovino, D., Madec, G., Masson, S., et al. (2010). Modifications of gyre circulation by sub-mesoscale physics. *Ocean Modelling*, *34*, 1–15. https://doi.org/10.1016/j.ocemod.2010.04.001
Locarnini, R., Mishonov, A., Antonov, J., Boyer, T., Garcia, H., Baranova, O., et al. (2010). *World Ocean Atlas 2009. Vol. 1, Temperature*. Washington, DC: U.S. Government Printing Office.
Lutjeharms, J. R. E. (2006). *The Agulhas current*. Berlin, Germany: Springer.
Marchesiello, P., Debreu, L., & Couvelard, X. (2009). Spurious diapycnal mixing in terrain-following coordinate models: The problem and a solution. *Ocean Modelling*, *26*, 156–169. https://doi.org/10.1016/j.ocemod.2008.09.004
Marchesiello, P., McWilliams, J. C., & Shchepetkin, A. F. (2001). Open boundary conditions for long-term integration of regional oceanic models. *Ocean Modelling*, *3*(1), 1–20. https://doi.org/10.1016/S1463-5003(00)00013-5
Marchesiello, P., McWilliams, J., & Schepetkin, A. (2003). Equilibrium structure and dynamics of the California Current System. *Journal of Physical Oceanography*, *33*, 753–783.
Matano, R., & Beier, E. J. (2003). A kinematic analysis of the Indian/Atlantic interocean exchange. *Deep Sea Research, Part II*, *50*(1), 229–249.
McWilliams, J. C. (1991). Geostrophic vortices. In *Non-linear topics in ocean physics, Proceedings of the international school of physics: Enrico Fermi"* (pp. 5–50). New York, NY: Course CIX, North Holland.
Molemaker, M. J., Mcwilliams, J. C., & Dewar, W. K. (2015). Submesoscale instability and generation of mesoscale anticyclones near a separation of the California undercurrent. *Journal of Physical Oceanography*, *45*, 613–629.
Morrow, R., Birol, F., Griffin, D., & Sudre, J. (2004). Divergent pathways of cyclonic and anti-cyclonic ocean eddies. *Geophysical Research Letters*, *31*, L24311. https://doi.org/10.1029/2004GL020974
Pascual, A., Faugre, Y., Larnicol, G., & Le Traon, P. (2006). Improved description of the ocean mesoscale variability by combining four satellite altimeters. *Geophysical Research Letters*, *33*, L02611. https://doi.org/10.1029/2005GL024633
Pegliasco, C., Chaigneau, A., & Morrow, R. (2015). Main eddy vertical structures observed in the four major Eastern Boundary Upwelling Systems. *Journal of Geophysical Research: Oceans*, *120*, 6008–6033. https://doi.org/10.1002/2015JC010950
Peliz, A., Boutov, D., Aguiar, A. B., & Carton, X. (2014). The Gulf of Cadiz Gap wind anticyclones. *Continental Shelf Research*, *91*, 171–191.
Piola, A. R., & Gordon, A. L. (1989). Intermediate waters in the southwest South Atlantic. *Deep Sea Research, Part A*, *36*(1), 1–16. https://doi.org/10.1016/0198-0149(89)90015-0
Reid, J. L. (1989). On the total geostrophic circulation of the South Atlantic Ocean: Flow patterns, tracers, and transports. *Progress in Oceanography*, *23*, 149–244. https://doi.org/10.1016/0079-6611(89)900013
Rhines, P. B. (1975). Waves and turbulence on a b plane. *Journal of Fluid Mechanics*, *69*, 417– 443.
Richardson, P. L., & Garzoli, S. L. (2003). Characteristics of intermediate water flow in the Benguela Current as measured with RAFOS floats. *Deep Sea Research, Part II*, *50*, 87–118. https://doi.org/10.1016/S0967-0645(02)00380-6
Rimaud, J., Speich, S., Blanke, B., & Nicolas, N. (2012). The exchange of Intermediate Water in the southeast Atlantic: Water mass transformations diagnosed from the Lagrangian analysis of a regional ocean model. *Journal of Geophysical Research*, *117*, C08034. https://doi.org/10.1029/2012JC008059
Rosso, I., Hogg McC, A., Strutton, P. G., Kiss, A. E., Matear, R., Klocker, A., et al. (2014). Vertical transport in the ocean due to sub-mesoscale structures: Impacts in the Kerguelen region. *Ocean Modelling*, *80*, 10–23. https://doi.org/10.1016/j.ocemod.2014.05.001
Roullet, G., Capet, X., & Maze, G. (2014). Global interior eddy available potential energy diagnosed from Argo floats. *Geophysical Research Letters*, *41*, 1651–1656. https://doi.org/10.1002/2013GL059004
Roullet, G., & Klein, P. (2010). Cyclone-anticyclone asymmetry in geophysical turbulence. *Physical Review Letters*, *104*, 218501.
Rubio, A., Blanke, B., Speich, S., Grima, N., & Roy, C. (2009). Mesoscale eddy activity in the southern Benguela upwelling System from satellite altimetry and model data. *Progress in Oceanography*, *83*(1), 288–295. https://doi.org/10.1016/j.pocean.2009.07.029
Rusciano, E., Speich, S., & Ollitrault, M. (2012). Interocean exchanges and the spreading of Antarctic Intermediate Water south of Africa. *Journal of Geophysical Research*, *117*, C10010. https://doi.org/10.1029/2012JC008266
Schmid, C., Boebel, O., Zenk, W., Lutjeharms, J. R. E., Garzoli, S. L., Richardson, P. L., et al. (2003). Early evolution of an Agulhas Ring. *Deep Sea Research, Part II*, *50*(1), 141–166.
Schouten, M. W., de Ruijter, W. P. M., van Leeuwen, P. J., & Ridderinkhof, H. (2003). Eddies and variability in the Mozambique Channel. *Deep Sea Research, Part II*, *50*(12–13), 1987–2003.
Shchepetkin, A. F., & McWilliams, J. C. (2003). A method for computing horizontal pressure-gradient force in an oceanic model with a non-aligned vertical coordinate. *Journal of Geophysical Research*, *108*(C3), 3090. https://doi.org/10.1029/2001JC001047
Shchepetkin, A. F., & McWilliams, J. C. (2005). The regional oceanic modeling System (ROMS): A split-explicit, free-surface, topography-following-coordinate oceanic model. *Ocean Modelling*, *9*, 304– 347. https://doi.org/10.1016/j.ocemod.2004.08.002
Smith, K. S. (2007). The geography of linear baroclinic instability in Earths oceans. *Journal of Marine Research*, *65*, 655–683.
Smith, W., & Sandwell, D. (1997). Global sea floor topography from satellite altimetry and ship depth soundings. *Science*, *277*(5334), 1956–1962. https://doi.org/10.1126/science.277.5334.1956
Soufflet, Y., Marchesiello, P., Lemarie', F., Jouanno, J., Capet, X., Debreu, L., et al. (2016). On effective resolution in ocean models. *Ocean Modelling*, *98*, 36–50.
Speich, S., Blanke, B., & Cai, W. (2007). Atlantic meridional overturning and the southern hemisphere supergyre. *Geophysical Research Letters*, *34*, L23614. https://doi.org/10.1029/2007GL031583
Speich, S., Lutjeharms, J. R. E., Penven, P., & Blanke, B. (2006). Role of bathymetry in Agulhas Current configuration and behaviour. *Geophysical Research Letters*, *33*, L23611. https://doi.org/10.1029/2006GL027157
Stewart, K. D., Hogg, A. M. C., Griffies, S. M., Heerdegen, A. P., Ward, M. L., Spence, P., et al. (2017). Vertical resolution of baroclinic modes in global ocean models. *Ocean Modelling*, *113*, 50–65. https://doi.org/10.1016/j.ocemod.2017.03.012
Talley, L. D. (1996). Antarctic intermediate water in the South Atlantic. In G. Wefer (Ed.), *The South Atlantic: Present and past circulation* (pp. 219–238). Berlin, Germany: Springer. https://doi.org/10.1007/978-3-642-80353-6-11
van Leeuwen, P. J., & de Ruijter, W. P. M. (2000). Natal pulses and the formation of Agulhas Rings. *Journal of Geophysical Research*, *105*, 6425–6436.
Weijer, W., de Ruijter, W. P. M., Dijkstra, H. A., & van Leeuwen, P. J. (1999). Impact of interbasin exchange on the Atlantic overturning circulation. *Journal of Physical Oceanography*, *29*, 2266–2284.